

Chiral magnetohydrodynamics with zero total chiralityAxel Brandenburg^{1,2,3,4}, Kohei Kamada⁵, Kyohei Mukaida^{6,7}, Kai Schmitz⁸, and Jennifer Schober⁹¹*Nordita, KTH Royal Institute of Technology and Stockholm University, 10691 Stockholm, Sweden*²*The Oskar Klein Centre, Department of Astronomy, Stockholm University, AlbaNova, SE-10691 Stockholm, Sweden*³*School of Natural Sciences and Medicine, Ilia State University, 0194 Tbilisi, Georgia*⁴*McWilliams Center for Cosmology and Department of Physics, Carnegie Mellon University, Pittsburgh, Pennsylvania 15213, USA*⁵*Research Center for the Early Universe (RESCEU), Graduate School of Science, The University of Tokyo, Hongo 7-3-1, Bunkyo-ku, Tokyo 113-0033, Japan*⁶*KEK Theory Center, Tsukuba 305-0801, Japan*⁷*Graduate University for Advanced Studies (Sokendai), Tsukuba 305-0801, Japan*⁸*Institute for Theoretical Physics, University of Münster, 48149 Münster, Germany*⁹*Institute of Physics, Laboratory of Astrophysics, École Polytechnique Fédérale de Lausanne (EPFL), 1290 Sauverny, Switzerland*

(Received 26 April 2023; accepted 22 August 2023; published 28 September 2023)

We study the evolution of magnetic fields coupled with chiral fermion asymmetry in the framework of chiral magnetohydrodynamics with zero initial total chirality. The initial magnetic field has a turbulent spectrum peaking at a certain characteristic scale and is fully helical with positive helicity. The initial chiral chemical potential is spatially uniform and negative. We consider two opposite cases where the ratio of the length scale of the chiral plasma instability (CPI) to the characteristic scale of the turbulence is smaller and larger than unity. These initial conditions might be realized in cosmological models, including certain types of axion inflation. The magnetic field and chiral chemical potential evolve with inverse cascading in such a way that the magnetic helicity and chirality cancel each other at all times, provided there is no spin flipping. The CPI timescale is found to determine mainly the time when the magnetic helicity spectrum attains negative values at high wave numbers. The turnover time of the energy-carrying eddies, on the other hand, determines the time when the peak of the spectrum starts to shift to smaller wave numbers via an inverse cascade. The onset of helicity decay is determined by the time when the chiral magnetic effect becomes efficient at the peak of the initial magnetic energy spectrum, provided the CPI does not grow much. When spin flipping is important, the chiral chemical potential vanishes at late times and the magnetic helicity becomes constant, which leads to a faster increase of the correlation length. This is in agreement with what is expected from magnetic helicity conservation and also happens when the initial total chirality is imbalanced. Our findings have important implications for baryogenesis after axion inflation.

DOI: [10.1103/PhysRevD.108.063529](https://doi.org/10.1103/PhysRevD.108.063529)**I. INTRODUCTION**

Relativistic plasmas are described by the evolution equations of chiral magnetohydrodynamics (MHD) [1–9]. Chirality enters in two distinct ways: first, through a nonvanishing chiral chemical potential, $\tilde{\mu}_5$, and second, through nonvanishing magnetic helicity density, $\mathbf{A} \cdot \mathbf{B}$, where $\mathbf{B} = \nabla \times \mathbf{A}$ is the magnetic field expressed in terms of the vector potential \mathbf{A} .

It has been known for some time that fermion chirality can be transferred into magnetic helicity and vice versa through the chiral anomaly [10,11]. The transfer of fermion chirality to magnetic helicity occurs through an instability [12] known as the chiral plasma instability (CPI) [13]. This instability is the fastest at a specific wave number, whose value depends on the chiral chemical potential. The transfer from magnetic helicity to chiral chemical potential does not involve any instability, but occurs just through a nonvanishing nonlinear source term in the evolution equation for the chiral chemical potential [3,14,15]. These differences in the evolutions of the chiral chemical potential and magnetic field can lead to nontrivial dynamics, which has triggered a lot of research [16–18]. Since fermion chirality is tightly related to the baryon and lepton

Published by the American Physical Society under the terms of the Creative Commons Attribution 4.0 International license. Further distribution of this work must maintain attribution to the author(s) and the published article's title, journal citation, and DOI. Funded by SCOAP³.

asymmetries at high temperature in the early Universe, their coevolution with magnetic helicity in the context of cosmology has also been extensively studied [19–27].

Previous investigations mostly assumed an initial imbalance between fermion chirality and magnetic helicity. In many investigations, the initial fermion chirality is non-vanishing while initial magnetic helicity is zero or vice versa. This can lead to a conversion of fermion chirality to a maximally helical magnetic field [3]. Also just spatial fluctuations can lead to magnetic field production [28,29]. Such chiral asymmetry, which can trigger the CPI, could be generated [30–32] in GUT baryogenesis in the early Universe [33–37] or weak interactions in compact stars [38–42] (see also Ref. [43] and references therein). However, numerical studies on other interesting initial conditions are still lacking, where fermion chirality is exactly opposite to magnetic helicity. Such an initial condition is expected if the chiral symmetry in the fermion sector is only broken through the topological density, $\partial_\mu J_5^\mu = -e^2 F_{\mu\nu} \tilde{F}^{\mu\nu} / (8\pi^2 \hbar^2 c)$, or the chiral anomaly [10,11], with J_5^μ being the chiral current and $e^2 F_{\mu\nu} \tilde{F}^{\mu\nu} / (8\pi^2 \hbar^2 c)$ being the topological density. Since the topological density can be written as a total derivative of the magnetic helicity density, the sum of chiral asymmetry and magnetic helicity vanishes when they are generated [44].

Configurations with vanishing total chirality are interesting not only in the context of chiral MHD, but also in particle physics and cosmology. At high enough temperatures, realized in the early Universe, the electron Yukawa interaction becomes inefficient for $T \gtrsim 10^5$ GeV [45,46]. There we find the conservation of total chirality because of $\partial_\mu J_{e_r}^\mu = -g_Y^2 Y_{\mu\nu} \tilde{Y}^{\mu\nu} / (16\pi^2 \hbar^2 c)$ with $J_{e_r}^\mu$ being the right-handed electron current and $Y^{\mu\nu}$ being the field strength of the hypercharge gauge field with gauge coupling g_Y . For instance, in a certain class of axion inflation, configurations with zero net chirality are generated during inflation [44], which can be the origin of the observed baryon asymmetry of the Universe [47–49] and it could explain the proposed intergalactic magnetic field; see, however, Ref. [26] for the baryon overproduction problem and Ref. [50] for the too large baryon isocurvature problem. The main purpose of this paper is to perform a full numerical chiral MHD simulation under the initial condition of vanishing total chirality and provide a better understanding of the non-linear dynamics in this case.

Before we begin our investigations, it is useful to recall the main findings of earlier work where the total chirality was mostly different from zero. Following the work of Ref. [14], who studied a system consisting of the gauge field and the chiral chemical potential, but without fluid velocity fields, and with the initial condition $\langle \mathbf{A} \cdot \mathbf{B} \rangle \neq 0$, $\tilde{\mu}_5 = 0$, three stages can be identified: (i) exponential decline of the magnetic helicity together with an increase of $\tilde{\mu}_5$, followed by (ii) a continued decrease of the typical peak wave number k_p , while $\tilde{\mu}_5$ stays at its

maximum value with $\langle \mathbf{A} \cdot \mathbf{B} \rangle$ being essentially zero, and (iii) a phase when all the fermion chirality $\tilde{\mu}_5$ gets transferred back to magnetic helicity. As expected, owing to magnetic helicity conservation, and because the magnetic field from the CPI is maximally helical, the magnetic energy density $\langle \mathbf{B}^2 \rangle / 2$ decays at late times such that $\langle \mathbf{B}^2 \rangle \xi_M \approx \text{const}$, where $\xi_M \equiv k_p^{-1}$ is the magnetic correlation length. In other words, both $\langle \mathbf{B}^2 \rangle$ and k_p decay in the same fashion, but, unlike the expected $t^{-2/3}$ scaling found previously for helical turbulence [51–54], the authors of Ref. [14] find a $t^{-1/2}$ scaling both for $\langle \mathbf{B}^2 \rangle$ and k_p . For sufficiently strong initial magnetic fields, the magnetic Reynolds number can be much larger than unity and the eddy turnover scale much longer than the estimated inverse peak momentum scale, if equipartition between the magnetic field and fluid velocity is established. This suggests that the effect of the fluid velocity cannot be negligible in general.

The earlier analytic study of Ref. [14] was revisited using direct numerical simulations of chiral MHD [15]. At large magnetic Reynolds numbers, the authors found clear evidence for a $t^{-2/3}$ scaling of both $\langle \mathbf{B}^2 \rangle$ and k_p at late times. They also found that the initial evolution is not exponential, as suggested in Ref. [14], but linear in time. However, they only considered the case where the initial fermion chirality was zero. When it is finite and balancing exactly the magnetic helicity, the magnetic field decays in a way similar to the case of a strong, nonhelical field [55], where the decay is governed by the conservation of the Hosking integral [56–58]. This integral describes the strength of magnetic helicity fluctuations on different length scales and has the dimensions of $\text{cm}^9 \text{s}^{-4}$, which implies the scalings $\xi_M \propto t^{4/9}$ and $\langle \mathbf{B}^2 \rangle \propto t^{-10/9}$ [56,58,59]. The general validity of the Hosking integral was further demonstrated by applying a corresponding analysis to the decay of a nonhelical magnetic field in neutron star crusts [60], where the magnetic field evolution is covered by the Hall effect [61].

Our goal here is to bridge the gap between the two extremes, where the initial chirality is either only in the fermions or only in the magnetic field, and to consider the intermediate case where fermion chirality and magnetic helicity balance to zero, extending the study of the present authors [55]. This is another case where the decay of $\langle \mathbf{B}^2 \rangle$ and k_p are described by a correspondingly adapted Hosking integral of the total chirality. In the following, we therefore refer to the Hosking integral with the chiral chemical potential included as the “adapted” Hosking integral; see Ref. [55] for detail.

As mentioned above, our findings on the evolution of the system with vanishing total chirality has significant impact on the present baryon asymmetry of the Universe. Another goal of the present paper is to clarify how the nontrivial coevolution of the magnetic field and fermion chirality affect the model space of axion inflation

consistent with the present Universe, which has not been explored before.

We begin, by presenting the basic equations and the mathematical setup of our simulations in Sec. II. We then discuss the parameter dependence of characteristic time-scales, consider the effect of spin flipping, and finally cases where the perfectly vanishing chirality balance is relaxed in Sec. III. Applications to the early Universe are discussed in Sec. IV. Conclusions are presented in Sec. V.

II. CHIRAL MAGNETOHYDRODYNAMICS

A. Chiral magnetic effect

Using Lorentz-Heaviside units, the Ampère-Maxwell equation for the QED-like model in the MHD limit (omitting the displacement current) reads

$$\nabla \times \mathbf{B} = \frac{1}{c} \mathbf{J}. \quad (1)$$

The electric current \mathbf{J} is the sum of the ohmic current and the chiral magnetic effect (CME) [62–64],

$$\mathbf{J} = \frac{\sigma}{c} (c\mathbf{E} + \mathbf{u} \times \mathbf{B}) + \frac{e^2}{2\pi^2 \hbar^2 c} \tilde{\mu}_5 \mathbf{B}, \quad (2)$$

where σ is the electric conductivity (or inverse magnetic diffusivity) and we consider the case with $\tilde{\mu}_5 \ll (e^2/\hbar c)k_B T$. By rewriting $c\mathbf{E} = -\partial\mathbf{A}/\partial t$ in the Weyl gauge, $e^2/4\pi\hbar c \equiv \alpha$, Eq. (2) is rewritten as

$$\frac{\partial\mathbf{A}}{\partial t} = \frac{c^2}{\sigma} (\mu_5 \mathbf{B} - \nabla \times \mathbf{B}) + \mathbf{u} \times \mathbf{B}, \quad (3)$$

where we defined [6]

$$\mu_5 \equiv \frac{2\alpha}{\pi\hbar c} \tilde{\mu}_5. \quad (4)$$

This expression agrees with Eq. (32) of Ref. [6], except for a factor of 2 resulting from a corresponding 1/2 factor in our adopted definition $\tilde{\mu}_5 = (\tilde{\mu}_R - \tilde{\mu}_L)/2$ in terms of the chemical potentials for right- and left-handed fermions [43]. The additional 4π factor in the numerator of the expression in Ref. [6] is a consequence of their use of cgs units.

B. Model description and basic equations

We perform simulations in a cubic domain of size L^3 with side lengths L and triply-periodic boundary conditions. The mass in the domain is therefore constant, so the mean density $\bar{\rho}$ is always equal to its initial value ρ_0 and put to unity in all cases. The lowest wave number in the domain is $k_1 = 2\pi/L$. Using N^3 mesh points, the largest wave number in the simulations is the Nyquist wave number $k_{\text{Ny}} = k_1 N/2$.

In the following, we set $c = 1$, so $\mathbf{J} = \nabla \times \mathbf{B}$. To include the effects of the cosmic expansion with scale factor $a(t) \propto t^{1/2}$ in the radiation-dominated era, which we assume to be a spatially flat Friedmann Universe, we use correspondingly scaled quantities and conformal time, $\eta(t) = \int dt/a(t)$, in which the evolution equations of MHD are the same as in the absence of expansion [65]. In order to obtain the physical quantities, we can simply normalize the corresponding comoving quantities with the appropriate powers of the scale factor a . Furthermore, using $\lambda = 3\hbar(2\alpha/\pi k_B T)^2$ and including spin flipping and spatial diffusion, our chiral anomaly equation is

$$\frac{\partial\mu_5}{\partial\eta} + \nabla \cdot (\mu_5 \mathbf{u}) = \frac{\lambda}{\sigma} (\mathbf{J} - \mu_5 \mathbf{B}) \cdot \mathbf{B} + D_5 \nabla^2 \mu_5 - \Gamma \mu_5, \quad (5)$$

where D_5 is an empirical diffusion coefficients for the chiral chemical potential. Here we used the relationship between the chiral chemical potential and the number density,

$$n_5 \equiv n_R - n_L = 2 \times \frac{\tilde{\mu}_5}{6\hbar^3} (k_B T)^2 = \frac{\pi\mu_5}{6\alpha\hbar^2} (k_B T)^2, \quad (6)$$

and used $J_5^\mu = (n_5, n_5 \mathbf{u} - D_5 \nabla n_5)$ for the chiral 4-current.

Owing to the chiral anomaly [10,11], the total chirality is conserved in the absence of spin flipping interaction [3,6]. It is then convenient to introduce the mean magnetic chirality equivalent as

$$\langle \mu_M \rangle \equiv \frac{1}{2} \lambda \langle \mathbf{A} \cdot \mathbf{B} \rangle, \quad (7)$$

so that the conservation law derived from Eqs. (3) and (5) can be stated in the form

$$\mu_{\text{tot}} = \langle \mu_5 \rangle + \langle \mu_M \rangle = \text{const.} \quad (8)$$

We complement Eqs. (3) and (5) by the momentum and continuity equations [6,7,66]

$$\begin{aligned} \frac{D\mathbf{u}}{D\eta} &= \frac{2}{\rho} \nabla \cdot (\rho \nu \mathbf{S}) - \frac{1}{4} \nabla \ln \rho + \frac{\mathbf{u}}{3} (\nabla \cdot \mathbf{u} + \mathbf{u} \cdot \nabla \ln \rho) \\ &\quad - \frac{\mathbf{u}}{\rho} [\mathbf{u} \cdot (\mathbf{J} \times \mathbf{B}) + \eta \mathbf{J}^2] + \frac{3}{4\rho} \mathbf{J} \times \mathbf{B}, \\ \frac{\partial \ln \rho}{\partial \eta} &= -\frac{4}{3} [\nabla + (\nabla \ln \rho)] \cdot \mathbf{u} + \frac{1}{\rho} [\mathbf{u} \cdot (\mathbf{J} \times \mathbf{B}) + \eta \mathbf{J}^2], \end{aligned} \quad (9)$$

where $D/D\eta \equiv \partial/\partial\eta + \mathbf{u} \cdot \nabla$ is the advective derivative, $\mathbf{S}_{ij} = (\partial_i u_j + \partial_j u_i)/2 - \delta_{ij} \nabla \cdot \mathbf{u}/3$ are the components of the rate-of-strain tensor, ν is the viscosity, and p is the pressure, which is assumed to be proportional to the density, i.e., $p = \rho c_s^2$, with $c_s = 1/\sqrt{3}$ being the sound speed for the ultrarelativistic fluid. The ratio of viscosity to magnetic diffusivity, $\nu\sigma$, is the magnetic Prandtl number,

which we choose to be unity in all cases. Likewise, we choose the ratio ν/D_5 to be unity in all cases.

For all our simulations, we use the PENCIL CODE [67], where the relevant equations are readily implemented. We use $N^3 = 1024^3$ mesh points for most of the runs, and $N^3 = 2048^3$ mesh points for one particular run. In a small number of cases, we have included the slope-limited diffusion (SLD) scheme of Ref. [68,69]. In those cases, SLD acts in addition to the ordinary viscous and diffusive processes stated in the equations above, but prevents the code from crashing during an early more violent phase when the mesh resolution is insufficient to dissipate the energy at high wave numbers. At later times, however, this additional numerical device has little effect. Below, we demonstrate in one case that the solutions with and without SLD yield the same result.

C. Diagnostic quantities

We introduce two characteristic times in our simulations, which are the timescale of the CPI and the magnetic diffusion time,

$$\eta_{\text{CPI}} = \sigma\mu_{50}^{-2} \quad \text{and} \quad \eta_{\text{diff}} = \sigma k_0^{-2}, \quad (10)$$

respectively. Here, k_0 is the initial value of the peak wave number k_p . The ratio $(\eta_{\text{diff}}/\eta_{\text{CPI}})^{1/2} = |\mu_{50}|/k_0$ characterizes the degree of scale separation between the scales of magnetic helicity and fermion chirality. We also define the turnover time of the energy-carrying eddies, which would determine the onset of turbulent inverse cascading,

$$\eta_{\text{turb}} = (u_{\text{rms}}^{\text{max}} k_0)^{-1}, \quad (11)$$

where $u_{\text{rms}}^{\text{max}}$ is the maximum value (in time) of the rms velocity.

Next, we introduce several parameters with a dimension of velocity. The nature of the CPI is characterized by the following parameters [7]

$$v_\lambda = |\mu_{50}|/(\bar{\rho}\lambda)^{1/2} \quad \text{and} \quad v_\mu = |\mu_{50}|/\sigma. \quad (12)$$

The former represents the ratio of the length scale of the magnetic field at saturation of the CPI to the CPI timescale, while the latter represents the ratio of the length scale of the initial instability to the CPI timescale. The ratio $v_\lambda/v_\mu = \sigma/(\bar{\rho}\lambda)^{1/2}$ characterizes the length of the k^{-2} spectrum that develops if the CPI operates without a strong pre-existing field [7]. In the unbalanced case, $u_{\text{rms}}^{\text{max}}$ is approximated by v_λ . In the present case, however, it does not seem to play any role. Instead, to compute $u_{\text{rms}}^{\text{max}}$, we approximate the velocity field by the initial magnetic field such that $B_{\text{rms}}^2 \simeq \bar{\rho}u_{\text{rms}}^2$. Using Eqs. (7) and (8), we estimate

$$B_{\text{rms}}^{(0)} \approx (k_0|\langle \mathbf{A} \cdot \mathbf{B} \rangle|)^{1/2} \approx \left(\frac{2k_0|\mu_{50}|}{\lambda} \right)^{1/2}, \quad (13)$$

which thus defines a new quantity \tilde{v}_λ as

$$\tilde{v}_\lambda \equiv \left(\frac{2k_0|\mu_{50}|}{\bar{\rho}\lambda} \right)^{1/2} \left(\approx \frac{B_{\text{rms}}^{(0)}}{\bar{\rho}^{1/2}} \right). \quad (14)$$

A predictive estimate for the turnover time of the energy-carrying eddies is thus

$$\eta_\lambda = (\tilde{v}_\lambda k_0)^{-1} = \left(\frac{\bar{\rho}\lambda}{2k_0^3|\mu_{50}|} \right)^{1/2}, \quad (15)$$

which is later used to predict the time when the inverse cascade sets in.

In this work, an important diagnostics is the magnetic energy spectrum, $E_M(k)$. It is normalized such that $\int E_M(k)dk = \langle \mathbf{B}^2 \rangle / 2 \equiv \mathcal{E}_M$ where \mathcal{E}_M is the magnetic energy density.¹ The kinetic energy spectrum $E_K(k)$ is defined similarly, i.e., $\int E_K(k)dk = \langle \rho u^2 \rangle / 2 \equiv \mathcal{E}_K$. We also define the magnetic helicity spectrum $H_M(k)$, which is normalized such that $\int H_M(k)dk = \langle \mathbf{A} \cdot \mathbf{B} \rangle$. In our simulations, $k|H_M(k)|/2$ approaches $E_M(k)$ near the maximum. In fact, the spectra $H_M(k)$ and $E_M(k)$ satisfy the realizability condition [70],

$$k|H_M(k)|/2 \leq E_M(k). \quad (16)$$

When this inequality is saturated for specific wave numbers, we say that the magnetic field is locally fully helical.

After some time, the magnetic helicity spectrum is characterized by two subranges, one with positive and one with negative values of $H_M(k)$, which are separated by the wave number $k_\pm(\eta)$, where the sign changes. In addition to the evolution of $k_\pm(\eta)$, we characterize the spectrum and its evolution by the numbers $k_I(\eta)$ and $k_{II}(\eta)$, which are the wave numbers of the first positive and second negative peak of $H_M(k)$.² The intermediate wave number $k_\pm(\eta)$ is numerically often better determined than $k_{II}(\eta)$, especially at early times.

The wave number of the first peak of the spectrum is close to the initial inverse correlation length,

$$\xi_M = \mathcal{E}_M^{-1} \int k^{-1} E_M(k) dk. \quad (17)$$

¹In terms of the mode function in the polarization basis, $\mathbf{A}(\mathbf{x}, t) \equiv \int d^3k / (2\pi)^{3/2} \sum_{\lambda=\pm} A_\lambda(\mathbf{k}, t) \mathbf{e}^\lambda(\mathbf{k}) e^{i\mathbf{k}\cdot\mathbf{x}}$, E_M is given as $E_M(k) = \sum_{s=\pm} (k^4/4\pi^2) |A_s(k)|^2$. We also have $H_M^s(k) = (k^3/2\pi^2) |A_s(k)|^2$ and $H_M(k) = (k^3/2\pi^2) \sum_{s=\pm} s |A_s(k)|^2$.

²In the present work, $k_I \approx k_p \equiv \xi_M^{-1}$, but the latter is based on the magnetic energy spectrum while the former is based on the magnetic helicity spectrum.

In fully helical turbulence, the value of $\xi_M(\eta)$ tends to increase with time in a power law fashion, $\xi_M \propto \eta^q$, where $q = 4/9$ in our cases of balanced chirality [55]; see also Sec. II E. Note that in our setup the positive helicity modes always dominate the energy density of the magnetic field, and hence approximately we have $\xi_M \simeq k_{\pm}^{-1}$.

It is convenient to introduce the mean magnetic chirality for the positive helicity modes for $k < k_{\pm}$ and the negative ones for $k > k_{\pm}$ as

$$\langle \mu_M^+ \rangle = \frac{\lambda}{2} \int_0^{k_{\pm}} H_M(k) dk, \quad (18)$$

$$\langle \mu_M^- \rangle = -\frac{\lambda}{2} \int_{k_{\pm}}^{\infty} H_M(k) dk. \quad (19)$$

The conservation law takes then the form

$$\langle \mu_5 \rangle + \langle \mu_M^+ \rangle - \langle \mu_M^- \rangle = \mu_{\text{tot}}, \quad (20)$$

where $\mu_{\text{tot}} = \mu_{50} + \mu_{M0} = \mu_{50} + \mu_{M0}^+ - \mu_{M0}^-$ is given by the initial values.

When we study the effect of spin flipping, we invoke a nonvanishing flipping rate with

$$\Gamma = \begin{cases} \Gamma_{\text{f0}} & \text{for } \eta_{\text{flip}} \leq \eta \leq \eta_{\text{off}} \\ 0 & \text{otherwise,} \end{cases} \quad (21)$$

where η_{flip} denotes the time when spin flipping is turned on, and in a few cases we allow for a finite value of η_{off} , which denotes the time when spin flipping is later turned off again. In the context of early Universe cosmology, we have indeed a constant flipping rate for the thermal Yukawa interaction [12]. A sudden turnoff is introduced for illustration, but such a transition can be realized by introducing new physics. Going into technical detail is beyond the scope of this paper.

D. Initial conditions

In our numerical experiments, the initial magnetic field is fully helical with positive magnetic helicity and random phases. The initial magnetic energy spectrum is a broken power law

$$E_M(k, \eta_0) \propto \begin{cases} k^4 & \text{for } k < k_0, \\ k^{-5/3} & \text{for } k > k_0, \end{cases} \quad (22)$$

where the initial peak is identified as $k_0 = k_1(\eta_0)$ and η_0 is the initial time. The IR spectrum is motivated by causality constraints [71], while the UV spectrum is taken as a Kolmogorov-type spectrum. The strength of the magnetic field is adjusted such that the initial magnetic chirality obeys $\mu_{M0} = -\mu_{50}$ such that $\mu_{\text{tot}} = 0$. The chiral chemical potential is initially assumed to be uniformly distributed in

space. Its initial value is always negative, i.e., $\mu_{50} < 0$. However, even for an initially uniform chiral chemical potential, there is a specific length scale associated with the value of μ_5 through the wave number of the most unstable mode of the CPI, $k = |\mu_{50}|/2$. The initial velocity is assumed vanishing in all cases.

E. Theoretical predictions

As was recently shown in Ref. [55], the present case of zero total chirality, where the magnetic helicity is canceled by fermion chirality, is remarkably similar to the case of ordinary MHD without chemical potential and zero magnetic helicity. In both cases, as already alluded to in the introduction, one can define a correlation integral of the total chirality, which is a quantity with dimensions $\text{cm}^9 \text{s}^{-4}$ and is dubbed the adapted Hosking integral. The evolution of the system can be explained by the conservation of this quantity. With a self-similar evolution of the magnetic spectrum being assumed, this yields the scalings $\xi_M \propto \eta^{4/9}$ and $\langle \mathbf{B}^2 \rangle \propto \eta^{-10/9}$ for the typical length scale and the magnetic energy density, respectively [56]. Note that the conservation of the adapted Hosking integral suggests

$$\xi_M^5 \langle \mathbf{B}^2 \rangle^2 = \text{const}, \quad \text{or} \quad k_1^{-3} E_M(k_1)^2 = \text{const}, \quad (23)$$

if the magnetic energy density is dominated by the positive helicity mode, which is peaked at $k = k_1$. For the magnetic field with an IR spectrum $\propto k^4$, as motivated from the causality constraints, the evolution of the magnetic field exhibits inverse cascading.

The big difference between ordinary MHD without helicity on the one hand and chiral MHD with helicity balanced by fermion chirality on the other hand is that in the latter, both the magnetic helicity and the fermion chirality are decaying, which we shall call *anomalous chirality cancellation* (ACC). In the former, by contrast, the Hosking integral based just on the ordinary magnetic helicity density is conserved. In the latter, contrary to the naively expected exponential decay of fermion chirality due to the CPI in chiral MHD, we actually have a much slower power-law decay proportional to $\eta^{-2/3}$, since the magnetic helicity is roughly estimated by $\xi_M \langle \mathbf{B}^2 \rangle$, and likewise for $|\langle \mu_5 \rangle|$ [55]. Here we have considered the case where the real space realizability condition of magnetic helicity [53], $|\mathcal{H}_M| \leq 2\mathcal{E}_M \xi_M$, is nearly saturated at ACC onset. Once this power law decay of the chirality starts, the CPI rate, $\langle \mu_5 \rangle^2 / \sigma$, decays faster than η^{-1} , which suggests that the CPI does not grow anymore. Hence, the magnetic energy is always dominated by helicity modes of the same sign as the initial ones, which, in our case, are positive helicity modes.

The adapted Hosking integral makes sense only when the communication between the helicity and chirality through the CME becomes effective at the characteristic scale. Therefore we expect that the scaling evolution

discussed above starts at the timescale of the CME at the peak scale. With the evolution equation for the magnetic field, equivalent to Eq. (3),

$$\frac{\partial \mathbf{B}}{\partial \eta} = \frac{1}{\sigma} [\nabla^2 \mathbf{B} + \nabla \times (\mu_5 \mathbf{B})] + \nabla \times (\mathbf{u} \times \mathbf{B}) \quad (24)$$

(where the second term in the right-hand side represents the CME), we estimate η_{ACC} as the time when the following condition is satisfied:

$$\eta_{\text{ACC}} \simeq \frac{\sigma}{\mu_5(\eta_{\text{ACC}})k_1(\eta_{\text{ACC}})}. \quad (25)$$

Note that from Eq. (24) we can also confirm that the magnetic field has an instability (the CPI) for one of the two circular polarization modes with $k = |\mu_{50}|/2$ being the most unstable mode. The instability rate is roughly given by μ_{50}^2/σ , which determines η_{CPI} .

The evolution of the system is classified into two cases, determined by the comparison between η_λ and η_{ACC} estimated by the initial conditions of k_1 and μ_5 . For relativistic plasmas with $\bar{\rho} \simeq (\pi^2 g_*/30)T^4$, where g_* is number of the relativistic degrees of freedom and $\sigma \simeq T/(\alpha \log \alpha^{-1})$ [72,73], we have $\eta_{\text{ACC}} < \eta_\lambda$ for $k_0 \ll |\mu_{50}|$ [more precisely, $k_0 \ll (\bar{\rho}\lambda/4\sigma^2)|\mu_{50}|$, which is independent of temperature], and vice versa. For $k_0 \ll |\mu_{50}|$, we have the following estimates for the evolution of the system:

- (1) The system is frozen when $\eta < \eta_{\text{CPI}}$.
- (2) The CPI starts to grow at $\eta \simeq \eta_{\text{CPI}}$.
- (3) If the CPI does not sufficiently amplify the negative helicity modes such that k_1 is unchanged, the chiral chemical potential starts to decay at $\eta = \eta_{\text{ACC}} (> \eta_{\text{CPI}})$ with

$$\eta_{\text{ACC}} \simeq \frac{\sigma}{|\mu_{50}|k_0} \quad (26)$$

in a mild way.

- (4) When $\eta \simeq \eta_\lambda (> \eta_{\text{ACC}})$, the system starts to evolve according to the scaling law found in Ref. [55],

$$k_1 \propto \eta^{-4/9}, \quad \mathcal{E}_M \propto \eta^{-10/9}, \quad \text{and} \quad (27)$$

$$\langle \mu_5 \rangle = -\langle \mu_M^+ \rangle + \langle \mu_M^- \rangle \propto \eta^{-2/3}. \quad (28)$$

In the case of mild hierarchy,³ $|\mu_{50}| \gtrsim k_0$, the case we mainly study in the next section, the assumption of inefficient CPI is guaranteed.

For $k_0 \gg |\mu_{50}|$, on the other hand, we expect the following evolution of the system.

³With ‘‘mild hierarchy’’, we have in mind a modest scale separation $|\mu_{50}|/k_0 = \mathcal{O}(10)$.

- (1) The system is frozen at $\eta < \eta_\lambda$.
- (2) The magnetic field evolves according to the inverse cascade at $\eta \simeq \eta_\lambda$ in a similar way as the usual inverse cascade for a nonchiral helical magnetic field,

$$k_1 \propto \eta^{-2/3}, \quad \mathcal{E}_M \propto \eta^{-2/3}, \quad \text{and} \quad (29)$$

$$\langle \mu_5 \rangle = -\langle \mu_M^+ \rangle + \langle \mu_M^- \rangle = \text{const}, \quad (30)$$

since the CME is not effective at $k \simeq k_1$ so that the magnetic helicity and chirality are individually conserved. Since k_1 decays, eventually it becomes smaller than $|\mu_5|$, and the system enters the regime similar to the previous case.

- (3) If the CPI does not sufficiently amplify the negative helicity modes, the CME becomes effective at $\eta \simeq \eta_{\text{ACC}} (> \eta_\lambda)$, which is now evaluated as

$$\eta_{\text{ACC}} \equiv \frac{\sigma^3}{|\mu_{50}|^3 k_0^3} \eta_\lambda^{-2} \simeq \frac{2\sigma^3}{\bar{\rho}\lambda\mu_{50}^2}. \quad (31)$$

Here, we have used Eq. (25) and $k_1(\eta) = k_0(\eta/\eta_\lambda)^{-2/3}$, as well as Eq. (14). When $\eta > \eta_{\text{ACC}}$ we have the inverse cascade with the conservation of the adapted Hosking integral,

$$k_1 \propto \eta^{-4/9}, \quad \mathcal{E}_M \propto \eta^{-10/9}, \quad \text{and} \quad (32)$$

$$\langle \mu_5 \rangle = -\langle \mu_M^+ \rangle + \langle \mu_M^- \rangle \propto \eta^{-2/3}. \quad (33)$$

Note that in this case, the CPI would not grow much due to the earlier onset of the chirality decay.

The assumption of inefficient CPI is guaranteed if the mild hierarchy $|\mu_5| \gtrsim k_1$ at η_{CPI} or η_{ACC} still holds. However, we have $|\mu_5|/k_1|_{\eta_{\text{CPI}}} = (2\sigma^2/\bar{\rho}\lambda)^{1/3}$, which is $\mathcal{O}(10^2)$ for the plasma of the Standard Model (SM) of particle physics with $\alpha \simeq 10^{-2}$ and $g_* \simeq 10^2$. In this case, there is a relatively large hierarchy between the chiral chemical potential and the peak scale of the magnetic field. We then might expect an earlier onset of the chirality decay triggered by the CPI. Namely, we have another possibility of the scaling law, which is a modification of step 3 discussed above, so we refer to it as step 3', i.e.,

- (3') After some epoch of the onset of CPI,

$$\eta \simeq \eta_{5\text{dec}} = c_A \eta_{\text{CPI}}, \quad \text{with} \quad c_A = \mathcal{O}(10), \quad (34)$$

the system enters the regime of the ACC. If the conservation of the adapted Hosking integral, with the rapid communication between the chirality and helicity through the CME, governs the evolution of the system, we would still have the scaling laws Eqs. (32) and (33), but the evolution nevertheless would have relatively large uncertainty, because of

TABLE I. Relevant timescales defined in this paper.

Timescale	Expression	Equation	Explanation
η_{CPI}	$\sigma\mu_{50}^{-2}$	Eq. (10)	Time scale of the CPI
η_{diff}	σk_0^{-2}	Eq. (10)	Magnetic diffusion time
η_{turb}	$(u_{\text{rms}}^{\text{max}} k_0)^{-1}$	Eq. (11)	Turnover time of the energy-carrying eddies
η_λ	$(\tilde{v}_\lambda k_0)^{-1} = [\bar{\rho}\lambda/(2k_0^3 \mu_{50})]^{1/2}$	Eq. (15)	<i>Predicted</i> turnover time of the energy-carrying eddies
η_{ACC}	$\sigma/[\mu_5(\eta_{\text{ACC}})k_{\text{I}}(\eta_{\text{ACC}})]$	Eq. (25)	Onset time of the ACC

the exponential instability from the CPI. For later purposes, we keep the ambiguity in the scaling evolution and introduce a scaling index q_5 such that

$$\langle\mu_5\rangle = -\langle\mu_{\text{M}}^+\rangle + \langle\mu_{\text{M}}^-\rangle \propto \eta^{-q_5}, \quad (35)$$

which will be used in Sec. IV.

In Table I, we summarize the characteristic timescales relevant for the evolution of the system; see Appendix A for a summary of additional timescales and wave numbers defined in this paper.

Some of the features described above will be confirmed by direct numerical simulations in Sec. III. They can have important consequences for baryon production, as will be discussed at the end of the paper.

III. RESULTS

In this section we show the results of the direct numerical simulation. We first study the case with $k_0 \ll |\mu_{50}|$ until Sec. III G. In Sec. III H we study the case with $k_0 \gg |\mu_{50}|$. Some of our observations will turn out to be consistent with the theoretical prediction discussed in Sec. II E. We will also see some other features that have not been addressed there.

A. Visualization of magnetic and fermion chiralities

We begin by discussing the simulation of Ref. [55] with $k_0 \ll |\mu_{50}|$, which we refer to as Run O. In Fig. 1, we present visual impressions of magnetic and fermion chiralities in Run O at different times. We see that the turbulent structures gradually grow in size and the extreme values away from zero decrease as time goes on. Furthermore, μ_5 and $\mathbf{A} \cdot \mathbf{B}\lambda/2$ have predominantly opposite signs, as expected. Locally, however, there is no correspondence between the two fields. This is because the vanishing total chirality is only a statistical property.

B. Evolution of characteristic scales

As discussed in Ref. [55], it is important to allow for sufficient scale separation between the smallest available wave number $k_{\text{I}} \equiv 2\pi/L$ and the initial wave number of the peak, k_0 . It is also important that there is enough separation

between k_0 and the initial wave number of the CPI, $|\mu_{50}|/2$, to confirm distinct features of the evolution of the system. Both, k_0 and $|\mu_{50}|/2$, in turn, must be much smaller than the largest available wave number $k_{\text{Ny}} = k_{\text{I}}N/2$. Sufficient scale separation between k_{I} and k_0 is particularly important for obtaining the theoretically expected increase of $\xi_{\text{M}} \propto \eta^{4/9}$ along with the decay of $\mathcal{E}_{\text{M}} \propto \eta^{-10/9}$, based on the conservation of the Hosking integral adapted to the total chirality. Indeed, in Run O, an optimized balance between the two scale separation requirements has been achieved.

With the start of the simulation, the helical random magnetic field, which is present initially, drives turbulent motions through the Lorentz force. This causes $E_{\text{K}}(k)$ to grow quickly at all wave numbers, but it is always less than $E_{\text{M}}(k)$; see Fig. 2, where we compare kinetic and magnetic energy spectra at different times. After some time, $E_{\text{K}}(k)$ approaches $E_{\text{M}}(k)$ at large values of k , i.e., the motions are in approximate equipartition with the magnetic field at high wave numbers. This observation supports the estimate of $u_{\text{rms}}^{\text{max}}$ for \tilde{v}_λ ; see Eq. (14). At the same time, the initial $k^{-5/3}$ spectrum for $E_{\text{M}}(k)$ develops into a slightly steeper one due to finite magnetic diffusion. In Fig. 2, we also mark the two scale separation ratios.

As already discussed in Ref. [55], even though there is vanishing net chirality, $\langle\mu_{\text{M}}\rangle + \langle\mu_5\rangle = 0$, there is still some degree of inverse cascading, just like in nonhelical magnetically dominated turbulence [54,74]. We see this clearly in Fig. 3, where the position of the magnetic peak, $k_{\text{I}}(\eta)$, gradually moves to smaller values. At the same time, the height of the peak decreases, following an approximate power law $\propto k^\beta$, with $\beta = 3/2$; see Fig. 3. This can be explained by the conservation of the Hosking integral [56,58]; see also Eq. (23). The exponent $\beta = 3/2$ is characteristic of the fact that the net chirality vanishes, even though near the peak itself the field is locally fully helical, as we see from the proximity of $k|H_{\text{M}}(k)|/2$ and $\mathcal{E}_{\text{M}}(k)$; see Eq. (16).

The newly injected magnetic helicity from the CPI leads to a growth of the magnetic field at large wave numbers. It manifests itself mostly through the build-up of negative magnetic helicity at high wave numbers. At some point, we also see a gradual propagation of the secondary peak k_{II} toward smaller k , which has not been addressed in Sec. II E.

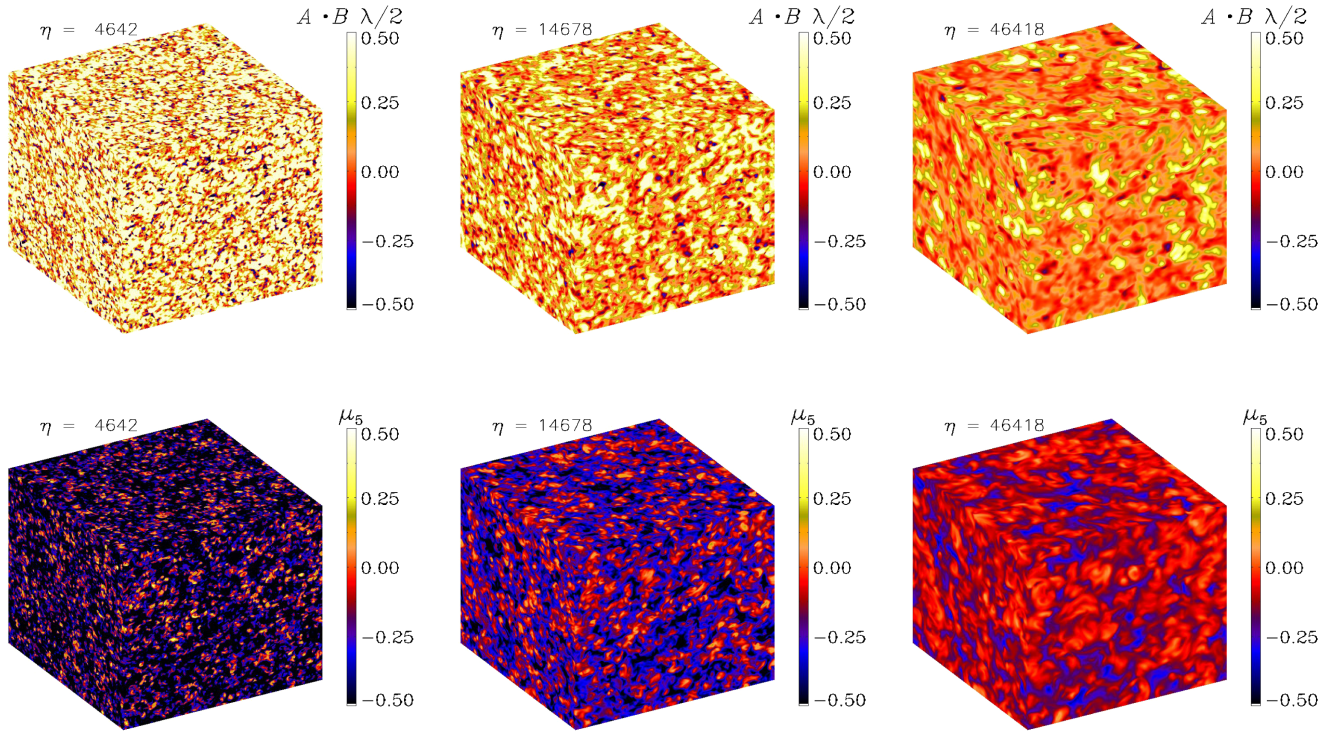


FIG. 1. Visualizations of $A \cdot B \lambda/2$ (upper row) and μ_5 (lower row) on the periphery of the computational domain for Run O at $\eta \approx 4600$ (left) 15,000 (middle), and 46,000 (right).

It lies underneath an envelope with an approximate $k^{8/3}$ slope; see Fig. 3. At present, the exponent $8/3$ is just empirical and there is no theory for it. It should be noted, however, that in other cases with a shorter inertial range, we have found larger exponents. Thus, the exponent could also

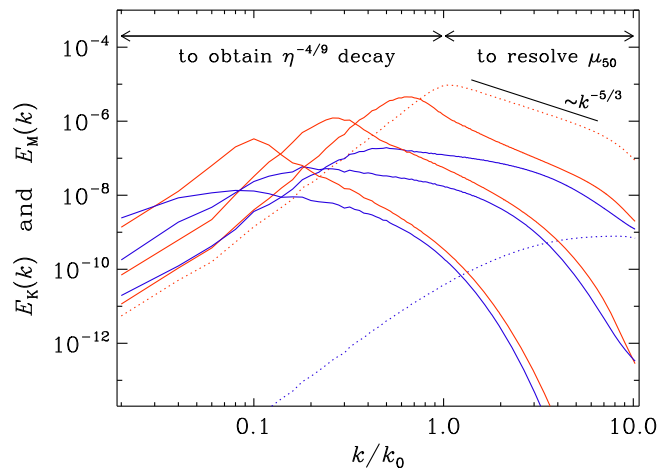


FIG. 2. Magnetic energy (red lines) and kinetic energy (blue lines) spectra for Run O at times $\eta = 460, 4600, \text{ and } 46,000$. The dotted lines denote the earliest outputted time $\eta = 0.3$. The straight black line indicates the initial $k^{-5/3}$ spectrum for the magnetic field. In the upper part, the two-sided arrows indicate the requirements for scale separation at small and large k to obtain the $k_p \propto \eta^{-4/9}$ decay and to resolve $|\mu_{50}|$, respectively.

be smaller when the inertial range is larger, i.e., when there is more scale separation and $\langle \mu_5 \rangle \xi_M$ is larger.

Another characteristic wave number is k_{\pm} , where the sign of the spectral magnetic helicity changes. It is used in the definitions of $\langle \mu_M^+ \rangle$ and $\langle \mu_M^- \rangle$ in Eqs. (18) and (19).

In Fig. 4 we plot the evolution of the characteristic wave numbers k_I , k_{\pm} , and k_{II} . We clearly see the $k_I \propto \eta^{-4/9}$ decay predicted by the conservation of the Hosking integral

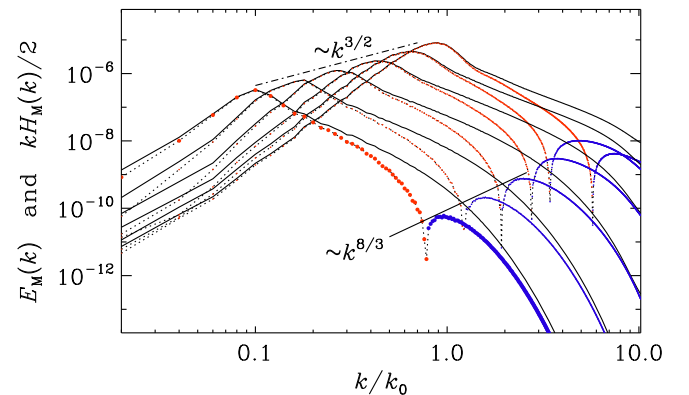


FIG. 3. Magnetic energy (solid lines) and normalized helicity spectra $kH_M(k)/2$ (dotted lines with red and blue symbols for positive and negative helicity spectra, respectively) for Run O at times $\eta = 150, 460, 1500, 4600, 15,000, \text{ and } 46,000$. The peaks k_I (peaks of the red curves) and k_{II} (peaks of the blue curves) evolve underneath the envelopes $\propto k^{3/2}$ and $\propto k^{8/3}$, respectively.

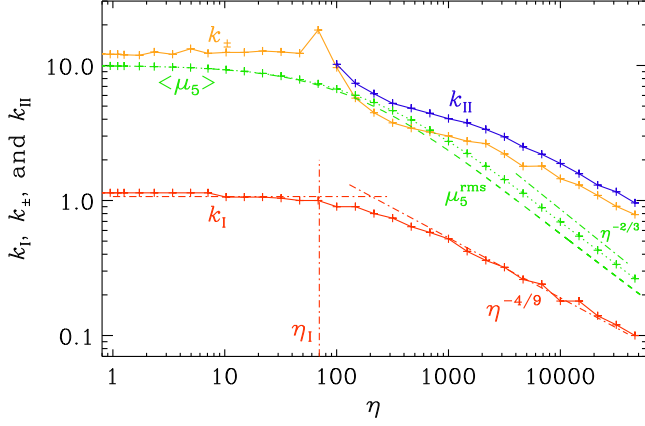


FIG. 4. Comparison of k_I (red), k_{\pm} (orange), and k_{II} (blue) for Run O. The green dashed line shows $\langle \mu_5 \rangle$ and the green dotted line shows the rms value μ_5^{rms} . The sloping red (green) dashed-dotted line indicates $\eta^{-4/9}$ ($\eta^{-2/3}$) scaling.

adapted to the total chirality [55]. It emerges after a time η_1 , which is expected to be close to η_λ (and also η_{turb}); see Eq. (15). In Run O we find $\eta_1 \approx 100$.

The evolution of k_{\pm} and k_{II} can be seen more clearly when the Nyquist wave number is larger. We therefore discuss in Fig. 5 another run, also with $N = 1024^3$ mesh points, but now with $k_1 = 0.05$ (instead of 0.02), so $k_{\text{Ny}} = 25.6$, which is a little over five times larger than $|\mu_{50}|/2 = 5$. In Table II, this run is referred to as Run I, which differs from the previously discussed Run O mainly in the value of k_1 . It also has a shallower scaling of the correlation length, $\xi_M \propto k_1^{-1} \propto \eta^{1/3}$, which seems to be an artifact caused by insufficient scale separation, i.e., the value of k_1 is not sufficiently small. Empirically, we find that, if $k_0/k_1 \gg 20$, there is an inverse cascade with

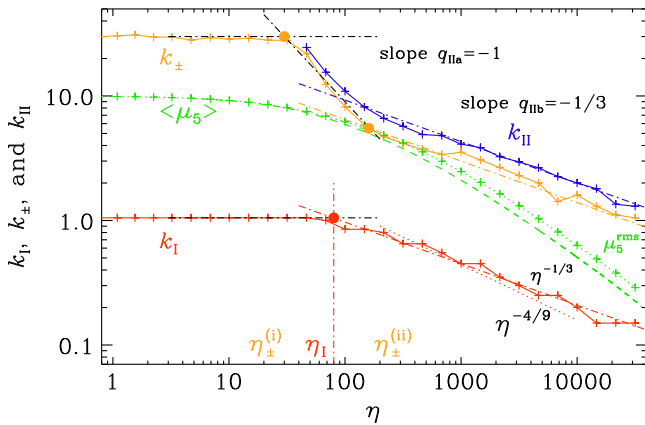


FIG. 5. Similar to Fig. 4, but for Run I. The red dashed-dotted line indicates here the $\eta^{-1/3}$ scaling, which describes the k_I scaling better than the $\eta^{-4/9}$ scaling indicated by the red dotted line. The orange and red dots indicate the crossings of the extrapolated tangents on which the times $\eta_{\pm}^{(i)}$, η_1 , and $\eta_{\pm}^{(ii)}$ are based.

$\xi_M \propto k_1^{-1} \propto \eta^{4/9}$. The parameters η_1 , $\eta_{\pm}^{(i)}$, and $\eta_{\pm}^{(ii)}$, listed in Table II, are discussed below. We also give here the values of v_μ and v_λ/v_μ . Run O' is similar to Run O, except that here, SLD has been added. The two runs are virtually indistinguishable.

The evolution of the peaks of the spectrum can be summarized as follows: (i) After the start of the run, the CPI induces a growth of the negative helicity modes at the secondary peak k_{II} , which stays constant until $\eta = \eta_{\pm}^{(i)}$, and then starts to decrease with time in a power law fashion, $k_{II} \propto \eta^{-q_{IIa}}$, with $q_{IIa} \approx 1$ in all cases; (ii) The original large-scale spectrum is unchanged until some time $\eta = \eta_1$ and then starts to decrease via an inverse cascade with $k_I(\eta) \propto \eta^{-q_I}$, where q_I is expected to be equal to the exponent $q = 4/9$ found in Ref. [55]; (iii) At time $\eta = \eta_{\pm}^{(ii)}$, the decay of the secondary peak becomes slower with a smaller index, $k_{II} \propto \eta^{-q_{IIb}}$, with $q_{IIb} < q_{IIa} \approx 1$. Those parameters are summarized in Table II.

The plot of characteristic wave numbers k_I , k_{\pm} , and k_{II} in Fig. 5 shows three distinct times, $\eta_{\pm}^{(i)} \lesssim \eta_1 \lesssim \eta_{\pm}^{(ii)}$, where k_{\pm} begins to decrease first rapidly, at $\eta = \eta_{\pm}^{(i)}$, and later, at $\eta = \eta_{\pm}^{(ii)}$, more slowly, approximately like $\eta^{-4/9}$, i.e., $q_{IIb} \approx q = 4/9$. The decay of k_{II} closely follows that of k_{\pm} . The decay of k_I , on the other hand, does not show the rapid decay phase that we see in k_{\pm} and k_{II} , but turns directly into the approximate $\eta^{-4/9}$ decay at $\eta = \eta_{\pm}^{(i)}$.

C. Onset of inverse cascading

It is of interest to vary the separation between $|\mu_{50}|/2$ and k_0 to see the dependence of the relevant characteristic times on these wave numbers. We have performed simulations for different values and consider runs where we change k_0 and keep μ_{50} fixed, and others where we change μ_{50} and keep k_0 fixed. It both cases, of course, since we want to satisfy $\langle \mu_5 \rangle + \langle \mu_M \rangle = \text{const}$, we need to adjust the amplitude of the initial magnetic field correspondingly. The results are summarized in Table II and plotted in Figs. 6 and 7.

One may presume that $\eta_{\pm}^{(i)}$ is roughly estimated by η_{CPI} since the grow of negative helicity modes becomes effective at that time. We see, however, that, while $\eta_{\pm}^{(i)}$ decreases quadratically with increasing $|\mu_{50}|$, the dependence on $\eta_{\text{CPI}} = \sigma \mu_{50}^{-2}$ is shallower than linear and follows approximately an $\eta_{\text{CPI}}^{2/3}$ scaling; see Fig. 6. Thus, k_{II} starts to decline more rapidly when $|\mu_{50}|$ is large, although it is unclear why this exponent is here $\approx 2/3$. On the other hand, we see that the five data points with $k_1 = 0.01$ (Runs L, M, N, J, and J' with smaller $|\mu_{50}|$) lie on another $\eta_{\text{CPI}}^{2/3}$ line that is shifted upward by a factor of about 6 relative to the runs with larger k_1 . The reason for this is that for large values of η_{CPI} , it became necessary to decrease the value of k_1 . This decreased the Nyquist wave number since N remained unchanged, which can cause artifacts in the values of k_{\pm} .

TABLE II. Summary of the runs discussed in this paper. Except for Run P, where $\lambda = 500$, we have in all other cases $\lambda = 2 \times 10^4$. Runs A and B below the last horizontal line have nonvanishing net chirality and are discussed at the end of the paper. The asterisk on the value of $k_1 = 0.01$ Run J* indicates that the resolution is $N^3 = 2048^3$, so the Nyquist wave number is here the same as for Run J* with $k_1 = 0.02$.

Run	k_0	$-\mu_{50}$	σ^{-1}	SLD	η_{CPI}	η_{diff}	$\eta_{N_0}^+$	q_1	η_{flip}	$\eta_{\pm}^{(i)}$	η_1	$\eta_{\pm}^{(ii)}$	$\eta_{N_0}^-$	$ \langle \mu_M^- \rangle ^{\text{max}}$	k_{\pm}/k_1	k_{Π}/k_1	v_{λ}	$u_{\text{rms}}^{\text{max}}$	k_1
VI	1	160	5×10^{-4}	No	0.08	2×10^3	3	1/3	...	0.3	45	14	7	43	1.4	2.0	1.13	0.095	0.2
V	1	80	5×10^{-4}	No	0.3	2×10^3	4	1/3	...	0.5	55	40	4	13	1.5	1.8	0.57	0.050	0.2
IV	1	50	5×10^{-4}	No	0.8	2×10^3	6	1/3	...	1.6	50	55	50	5.1	1.5	2.0	0.35	0.050	0.1
III	1	30	5×10^{-4}	No	2.2	2×10^3	14	1/3	...	1.7	80	108	150	1.5	1.8	2.3	0.21	0.018	0.2
II+	1	20	5×10^{-4}	No	5	2×10^3	18	1/3	...	6	75	160	200	0.46	1.8	3.1	0.141	0.031	0.1
II	1	20	2×10^{-4}	No	12.5	5×10^3	60	1/3	...	9	75	120	200	0.009	4.4	6.7	0.141	0.032	0.1
II-	1	20	1×10^{-4}	No	25	1×10^4	160	1/3	...	14	75	140	200	0.003	6.7	10	0.141	0.031	0.1
I	1	10	2×10^{-4}	No	50	5×10^3	125	1/3	...	30	80	160	250	0.009	6.7	9.6	0.071	0.030	0.05
O	1	10	2×10^{-4}	No	50	5×10^3	125	4/9	...	20	70	120	300	0.008	8.1	9.6	0.071	0.0123	0.02
O'	1	10	2×10^{-4}	Yes	50	5×10^3	125	4/9	...	20	110	120	400	0.015	6.4	8.4	0.071	0.0103	0.02
L	1	10	2×10^{-4}	Yes	50	5×10^3	125	4/9	...	180	400	500	1000	0.027	6.7	8.7	0.071	0.0079	0.01
M	1	7	2×10^{-4}	Yes	102	5×10^3	165	1/3	...	260	220	800	800	0.006	5.8	7.2	0.049	0.0065	0.01
N	1	5	2×10^{-4}	Yes	200	5×10^3	235	1/3	...	350	200	800	1000	0.0015	6.3	7.8	0.035	0.0055	0.01
N'	1	5	2×10^{-4}	Yes	200	5×10^3	200	4/9	800	3000	15000	0.00004	5.5	2.4	0.035	0.0035	0.0005
F	1	5	2×10^{-4}	Yes	200	5×10^3	...	4/9	100	...	250	9000	30	30	0.035	0.0055	0.01
J	1	5	5×10^{-4}	No	80	2×10^3	71	4/9	...	230	300	500	700	0.0003	6.1	7.6	0.035	0.0068	0.01
J*	1	5	5×10^{-4}	No	80	2×10^3	71	4/9	...	90	300	500	460	0.0006	6.1	7.6	0.035	0.0071	0.01*
J'	1	5	5×10^{-4}	No	80	2×10^3	76	1/3	...	95	120	500	460	0.0005	5.8	7.7	0.035	0.0070	0.02
P	1	0.1	2×10^{-4}	No	5×10^5	5×10^3	10^4	3/5	160	3×10^{-9}	0.001	0.0070	0.02
G	0.5	10	2×10^{-4}	No	50	2×10^{-4}	200	1/3	...	30	360	360	300	0.044	4.6	6.6	0.071	0.0188	0.05
H	0.2	10	2×10^{-4}	No	50	1.2×10^5	375	1/3	...	75	2000	2000	3000	0.42	2.0	2.7	0.071	0.0074	0.02
A	1	10	2×10^{-4}	No	50	5×10^3	...	4/9	...	8	110	210	7.3	9.5	0.071	0.0109	0.02
B	1	10	2×10^{-4}	No	50	5×10^3	...	4/9	...	20	90	120	250	...	7.8	8.9	0.071	0.0137	0.02

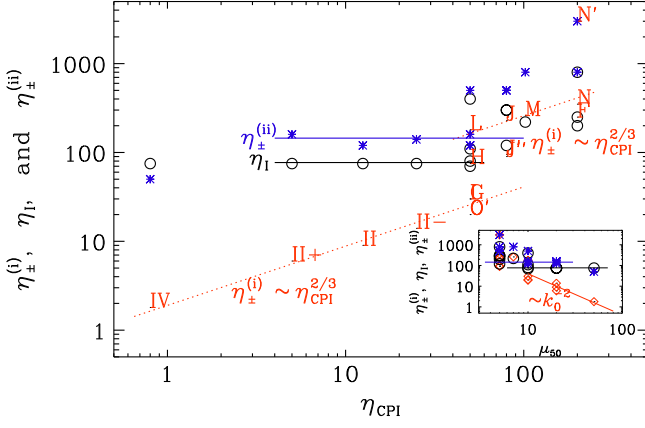


FIG. 6. Dependence of $\eta_{\pm}^{(i)}$, η_I , and $\eta_{\pm}^{(ii)}$ on η_{CPI} . $\eta_{\pm}^{(i)}$ shows an approximate $\eta_{\text{CPI}}^{2/3}$ dependence along two branches that are separated by a factor of about 6. η_I and $\eta_{\pm}^{(ii)}$ are essentially independent of η_{CPI} . The inset shows that $\eta_{\pm}^{(i)}$ scales inverse quadratically with $|\mu_{50}|$.

Small values of k_1 also facilitates the $\eta^{4/9}$ scaling of ξ_M and related length scales; see the comparison between Runs N and N' in Table II. This shows that $\eta_{\pm}^{(i)}$ is currently very sensitive to these restrictions which will be alleviated in future with larger computational power. Nevertheless, there

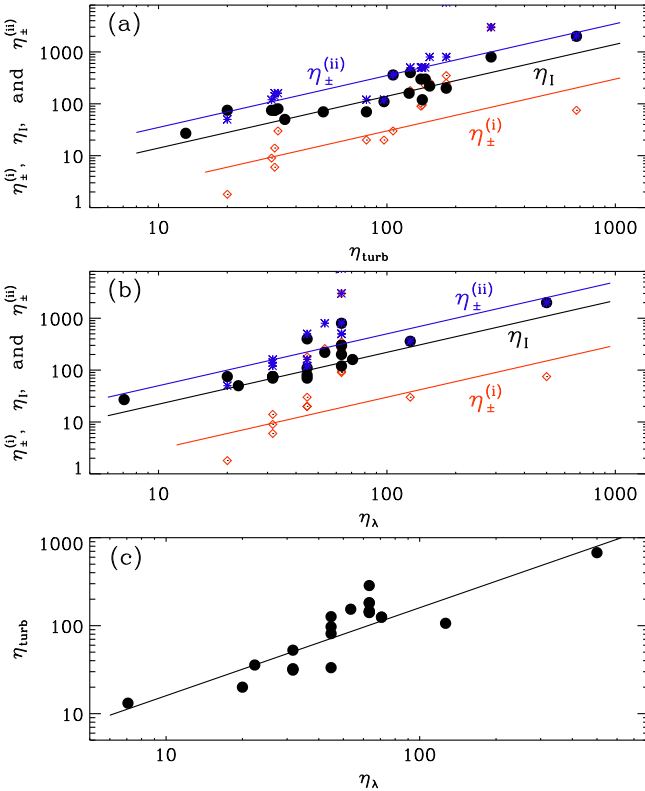


FIG. 7. Dependence of $\eta_I \approx \eta_{\pm}^{(ii)}$ and $\eta_{\pm}^{(i)}$ on (a) η_{turb} and (b) η_{λ} , as well as (c) the dependence of η_{turb} on η_{λ} .

is clearly a trend for an uprise in the dependence of $\eta_{\pm}^{(i)}$ on η_{CPI} for large values.

Next, we examine the dependence of η_I and $\eta_{\pm}^{(ii)}$ on k_0 and μ_{50} . Figure 6 shows that the time η_I of the onset of the decline of k_1 does not strongly depend on the value of μ_{50} . Likewise, the time $\eta_{\pm}^{(ii)}$ when the decay of k_{II} slows down, does not strongly depend on μ_{50} . Again, however, there is an upward shift of data points for the four runs, for which $k_1 = 0.01$. As discussed in Sec. II E, we expect that η_I is close to η_{turb} and η_{λ} . The upper two panels of Fig. 7 show the dependence of $\eta_{\pm}^{(i)}$, η_I , and $\eta_{\pm}^{(ii)}$ on η_{turb} and η_{λ} , respectively. From these plots, we estimate that

$$\eta_I \approx 1.4\eta_{\text{turb}} \approx 2.2\eta_{\lambda}. \quad (36)$$

In the lowest panel of Fig. 7, we also show the relation between η_{turb} and η_{λ} , i.e.,

$$\eta_{\text{turb}} \approx 1.6\eta_{\lambda}, \quad (37)$$

which shows the validity of the estimate of $u_{\text{rms}}^{\text{max}}$ in terms of \tilde{v}_{λ} . Equation (36) is useful for estimating the properties of magnetic field strength and coherence length at later times. Therefore, we conclude that the numerical results support, at least for a moderate scale separation, $1 < |\mu_{50}|/k_0 \lesssim \mathcal{O}(10)$, the theoretical estimate for the evolution of the characteristic scales given in Sec. II E with a more accurate determination of the time of the onset of the scaling evolution, Eq. (36).

D. Evolution of $\langle \mu_5 \rangle$ and $\langle \mu_M^{\pm} \rangle$

We now discuss how the chirality of the system evolves. Using Eqs. (18) and (19), we divide the magnetic helicity into $\langle \mu_M^+ \rangle$ and $\langle \mu_M^- \rangle$. The typical evolution of $\langle \mu_5 \rangle$ and $\langle \mu_M^{\pm} \rangle$ is as follows: (i) $\langle \mu_5 \rangle$ and $\langle \mu_M^+ \rangle$ stay constant until the time $\eta = \eta_{\mu_M^+}$, when the ACC commences exhibiting a power law decay; (ii) $\langle \mu_M^- \rangle$ grows until the time $\eta = \eta_{\mu_M^-}$ and then decays. Thus, $\eta_{\mu_M^-}$ is determined as the time when $\langle \mu_M^- \rangle$ is maximum.

As discussed in Sec. II E, the decay of $\langle \mu_5 \rangle$ and $\langle \mu_M^+ \rangle$ due to the ACC is expected to be like $\eta^{-2/3}$. In Fig. 8, we have overplotted the asymptotic $\eta^{-2/3}$ decay laws of magnetic helicity with results of some of the representative numerical runs (Runs II, J, and G), which clearly shows that the numerical results support the theoretical prediction.

The decay of $\langle \mu_M^- \rangle$ is faster than that of $\langle \mu_5 \rangle$ and $\langle \mu_M^+ \rangle$ and follows an approximate $\eta^{-4/3}$ law, resulting in a decay of the ratio $\langle \mu_M^- \rangle / \langle \mu_M^+ \rangle \propto \eta^{-2/3}$. Therefore, unless $\langle \mu_M^- \rangle$ becomes comparable to $\langle \mu_M^+ \rangle$ when the growth stops, a complete cancellation between $\langle \mu_M^- \rangle$ and $\langle \mu_M^+ \rangle$ never occurs.

The production of $\langle \mu_M^- \rangle$ is expected to be a result of the CPI. We now address the question of how much $\langle \mu_M^- \rangle$ is being produced and what its maximum value depends on.

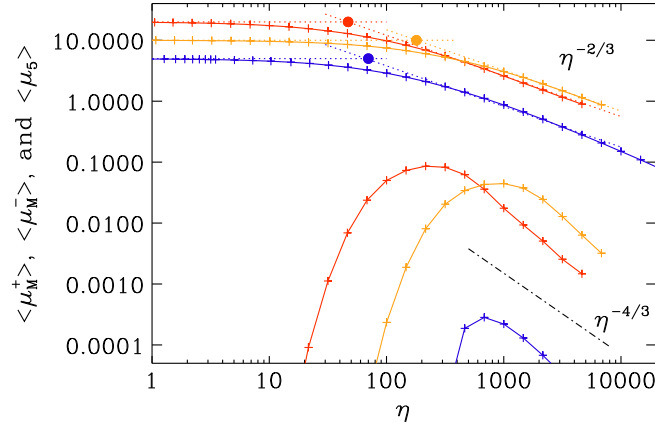


FIG. 8. Comparison of $\langle \mu_{\pm}^{\pm} \rangle$ for Run II (red lines), Run J (blue lines), and Run G (orange lines). The times η_{ACC} are marked by the correspondingly colored-filled symbol at the crossing points of the extrapolated $\eta^{-2/3}$ decay law with the initially constant values, indicated by dotted line. The $\eta^{-4/3}$ decay law $\langle \mu_{\text{M}}^{-} \rangle$ is shown as the dashed-dotted line.

Figure 8 shows that $\langle \mu_{\text{M}}^{-} \rangle$ is generally rather small, and at least for $\mu_{50}/k_0 \lesssim 20$ there is always a strong imbalance between $|\langle \mu_{\text{M}}^{+} \rangle|$ and $|\langle \mu_{\text{M}}^{-} \rangle|$, which never enters a phase with a near-complete cancellation.

To see whether this is related to the value of the conductivity, we compare simulations with different values of σ . It turns out that runs with smaller magnetic diffusivity ($\sigma^{-1} = 10^{-4}$) result in an even larger imbalance, while those with a larger diffusivity ($\sigma^{-1} = 5 \times 10^{-4}$) have a smaller imbalance; compare Runs II+, II, and II– in Table II.

Before closing this section, let us comment on another trend in the numerical runs we conducted regarding the absence of a near-complete cancellation between $\langle \mu_{\text{M}}^{-} \rangle$ and $\langle \mu_{\text{M}}^{+} \rangle$. For Runs III–VI, the ratio $|\langle \mu_{\text{M}}^{-} \rangle|^{\text{max}}/|\mu_{50}|$ becomes rather large. This could be due to the very large scale separation of k_0 and $|\mu_{50}|$. This suggests a possibility that the CPI completes the cancellation between the magnetic helicity and chirality immediately. However, the positive and negative helicity modes are distributed at separate length scales with the negative ones sitting at higher length scales and the latter receives a stronger magnetic diffusion. Therefore we expect the cancellation not to be complete and that the two helicity modes decay with a power-law decay, not an exponential one, though the scaling index can be different from $-2/3$. In order to investigate the evolution of the system in such extreme cases, $|\mu_{50}|/k_0 \gg \mathcal{O}(10)$, we need to have a sufficiently large box size to realize the corresponding scale separation. The detailed study is left for future study.

E. Onset of ACC

In Fig. 9, we show the dependence of $\eta_{\mu_{\text{M}}^{+}}$ and $\eta_{\mu_{\text{M}}^{-}}$ on $\eta_{\text{ACC}} = \sigma/|\mu_{50}k_0|$ [for the case $k_0 \ll |\mu_{50}|$; see Eq. (26)]. It

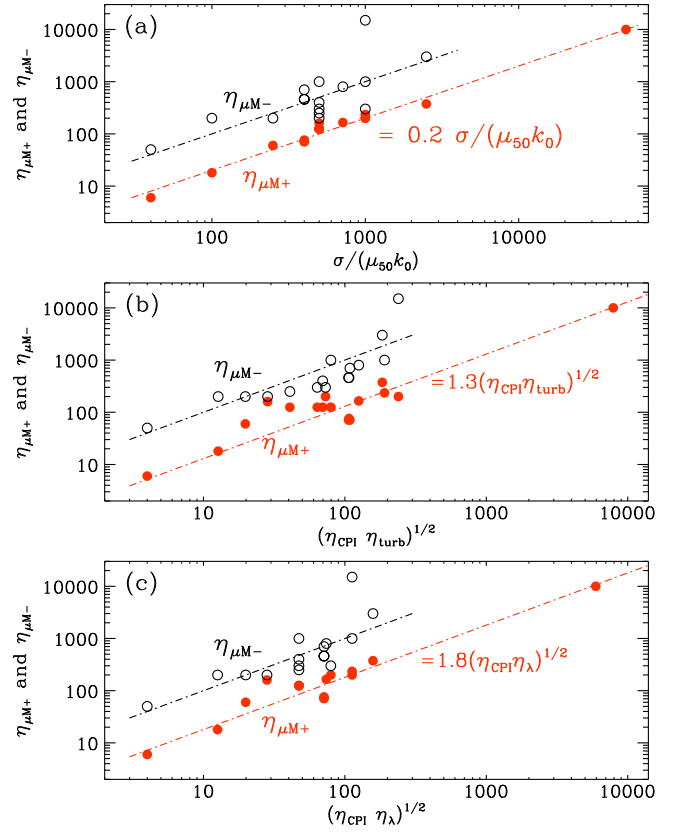


FIG. 9. Dependence of $\eta_{\mu_{\text{M}}^{+}}$ and $\eta_{\mu_{\text{M}}^{-}}$ on (a) $\sigma/|\mu_{50}k_0|$ as well as the geometric means of η_{CPI} and (b) either η_{turb} or (c) η_{λ} .

turns out that $\eta_{\mu_{\text{M}}^{+}}$ increases with $\eta_{\text{ACC}} = \sigma/|\mu_{50}k_0|$ such that

$$\eta_{\mu_{\text{M}}^{+}} \approx 0.2\eta_{\text{ACC}} = 0.2\sigma/|\mu_{50}k_0| \quad (38)$$

provides a good description to the data, which supports the discussion in Sec. II E, at least for a mild hierarchy $|\mu_{50}| \gtrsim k_0$. Furthermore, $\eta_{\mu_{\text{M}}^{-}}$ shows an approximately linear dependence on η_{ACC} . This is reasonable because the CPI becomes ineffective when the ACC onsets such that $\langle \mu_{\text{M}}^{-} \rangle$ is no longer amplified by the CPI after that.

F. The scale ratios k_{\pm}/k_{I} and $k_{\text{II}}/k_{\text{I}}$

We also mention another observation in the case with $k_0 \ll |\mu_{50}|$. At late times, the scale ratios k_{\pm}/k_{I} and $k_{\text{II}}/k_{\text{I}}$ reach values that are approximately constant in time. It is about 10 in the case of Run O, i.e., equal to the initial scale separation, $|\mu_{50}|/k_0 = 10$. One might have expected the scale ratios to increase with $|\mu_{50}|/k_0$. However, in all other cases, this ratio is smaller. Some of this might also be caused by one of the two scale-separation constraints not being well-enough obeyed, although the counterintuitive trend remains surprising.

In Fig. 10, we show the ratios k_{\pm}/k_{I} and $k_{\text{II}}/k_{\text{I}}$ versus $|\mu_{50}|/k_0 = (\eta_{\text{diff}}/\eta_{\text{CPI}})^{1/2}$. The two insets give separately

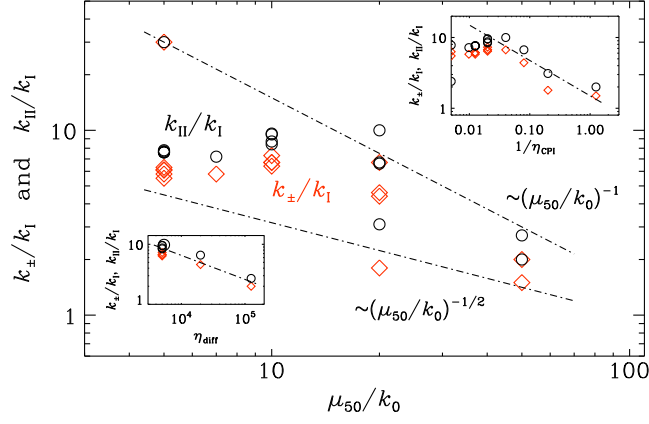


FIG. 10. Dependence of k_{\pm}/k_1 and k_{\parallel}/k_1 on η_{CPI} , showing an $\eta_{\text{CPI}}^{-0.4}$ behavior. on η_{diff} , showing a $\propto \eta_{\text{diff}}^{-1}$ behavior.

the dependencies on $1/\eta_{\text{CPI}}$, showing an $\eta_{\text{CPI}}^{-0.4}$ behavior, and on η_{diff} , with a $\propto \eta_{\text{diff}}^{-1/2}$ behavior. We see that k_{\pm}/k_1 and k_{\parallel}/k_1 decrease both with $1/\eta_{\text{CPI}}$ and with η_{diff} , giving a combined dependence on just the ratio $|\mu_{50}|/k_0$. Thus, we see that, somewhat unexpectedly, large $|\mu_{50}|$ and small k_0 tend to be detrimental to producing large scale ratios.

G. Effect of chirality flipping

The simulations discussed so far had $\Gamma = 0$ and they resulted in a final state where $\langle \mu_5 \rangle$ and $\langle \mu_M \rangle$ vanish at late times. As discussed in the introduction, spin flipping could prematurely lead to a vanishing $\langle \mu_5 \rangle$, which would imply that the decay of $\langle \mu_M \rangle$ would slow down and level off at a value away from zero. To study this quantitatively, we show in Fig. 11 the evolution of $\langle \mu_5 \rangle$, $\langle \mu_M \rangle$, and $\langle \mu_5 \rangle + \langle \mu_M \rangle$ for Run F with $\eta_{\text{flip}} = 100$ and $\Gamma_{f0} = 10^{-2}$ either for the rest of the run or only until $\eta_{\text{off}} = 10^3$ (Run F in Table II). We expect that if chirality flipping becomes effective much later than the ACC, we do not see the effect of chirality flipping, while if it becomes effective much earlier, we do not see the ACC. This is demonstrated in Appendix B, where we show spin-flipping versions of Runs VI and P, where $\eta_{\text{ACC}} \ll \eta_{\text{flip}}$ and $\eta_{\text{ACC}} \gg \eta_{\text{flip}}$, respectively. Thus we choose the parameter such that the chirality flipping becomes effective around (or somewhat before) the time of onset of the ACC to capture the behavior of the system at an intermediate stage.

First, we study a case where spin flipping acts permanently (after $\eta = \eta_{\text{flip}}$), which is shown in Fig. 11 as solid lines. We see that $|\langle \mu_5 \rangle|$ begins to decrease rapidly to zero after $\eta_{\text{flip}} = 100$. This slows down the decay of $\langle \mu_M \rangle$, which then declines at a much smaller rate; compare with the evolution for Run N, which is similar to Run F, but without spin flipping. Qualitatively similar behaviors are also seen for smaller values of Γ_{f0} . In all cases, we see that $\langle \mu_5 \rangle + \langle \mu_M \rangle$ evolves away from zero. This is because the total chirality is then no longer conserved. The decay of $\langle \mu_M \rangle$ is

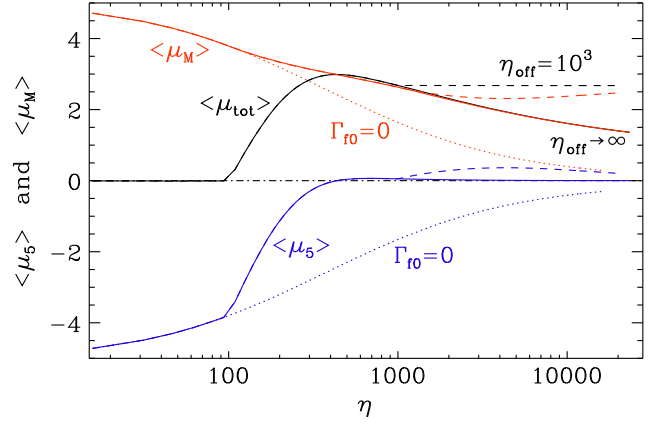


FIG. 11. Evolution of $\langle \mu_M \rangle$ (red), $\langle \mu_5 \rangle$ (blue), and their sum (black) for Run F with $\eta_{\text{flip}} = 100$ and $\Gamma_{f0} = 10^{-2}$ either for the rest of the run or only until $\eta_{\text{off}} = 10^3$. The dotted lines correspond to Run N without spin flipping.

understood by magnetic diffusion. Thus, we expect the decrease to slow down for a larger-scale separation between the magnetic diffusion scale and k_1 .

Next, it is also of interest to study a case where spin flipping acts only for a certain time interval and is then turned off again at $\eta = \eta_{\text{off}}$. This case is shown in Fig. 11 as dashed lines. We see that, when $\Gamma = 0$ after $\eta_{\text{off}} = 10^3$, the sum $\langle \mu_5 \rangle + \langle \mu_M \rangle$ is strictly constant and away from zero. This is in contrast to the case with permanently non-vanishing Γ_{f0} , where the sum continues to decrease slowly. The constancy of the total chirality leads to the behavior that $\langle \mu_M \rangle$ stops to decline rapidly at a larger value. Furthermore, during that time, some of the magnetic helicity decays due to the magnetic diffusion and is temporarily converted back into fermion chirality through the total chirality conservation; see the small increase of $\langle \mu_5 \rangle$ with a positive maximum at $\eta \approx 4000$ in Fig. 11. Later, however, this excess fermion chirality gets converted back into magnetic fields, which explains the slight uprise of $\langle \mu_M \rangle$ near the end of the simulation. Indeed, this process is similar to the one seen in Refs. [14,15]. This is natural because after the decay of $\langle \mu_5 \rangle$ the setup becomes very similar to the ones in these studies.

In Fig. 12, we show $\eta_{\pm}^{(i)}$ and η_{I} in the presence of spin flipping. The results suggests that the $\eta^{-4/9}$ decay changes into the faster $\eta^{-2/3}$ decay. Spin flipping brings $\langle \mu_5 \rangle$ close to zero. This process stops or slows down the decline of magnetic helicity, which therefore remains positive. At late times, $\langle \mu_5 \rangle$, which was originally negative, now becomes positive and settles at a value of around $\langle \mu_5 \rangle \approx k_1$. This is because at later times the positive chirality induced due to the helicity decay by the magnetic diffusion through the chiral anomaly is balanced by the erasure of the chirality through the CME [14,15], similar to the baryon asymmetry through the magnetic helicity decay much before the electroweak phase transition [19,20,24].

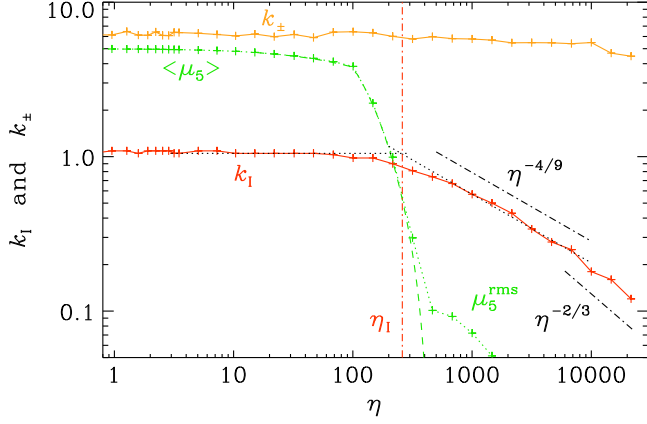


FIG. 12. $k_{\pm}^{(i)}$ and k_1 for Run F with spin flipping, $\eta_{\text{flip}} = 100$ and $\Gamma_{f0} = 10^{-2}$ for the rest of the run. As in Fig. 4, the green dashed line shows $\langle \mu_5 \rangle$ and the green dotted line shows μ_5^{rms} .

The sign of the final value of $\langle \mu_5 \rangle$ is determined by the magnetic helicity after the decay of $\langle \mu_5 \rangle$ due to the onset of spin flipping. In the cases presented above, the sign of the magnetic helicity at the time of the onset of spin flipping was positive and thus the chiral chemical potential at later times was also positive. If the initial magnetic field is weaker and the total chirality being negative (see Appendix C), the sign of the final value of $\langle \mu_5 \rangle$ can stay negative.

Our runs show that spin flipping can lead to a significant increase of the fraction of the magnetic helicity that can be preserved in spite of the fact that the system has vanishing total chirality. This also reduces the total energy-density dissipation of the system. In the absence of spin flipping, both magnetic helicity and chiral chemical potential would approach zero, so there would be no magnetic helicity available for successful baryogenesis. In the real Universe, however, spin flipping due to the electron Yukawa interaction, which really violates the (total) chirality conservation, inevitably acts at $T \lesssim 10^2$ TeV [45,46], and hence magnetic helicity survives more or less at the electroweak phase transition.

In Fig. 12, we see an interval between the onset of spin flipping, $\eta = \eta_{\text{flip}} = 10^2$, and the onset of the $\eta^{-2/3}$ scaling evolution of k_1 , $\eta \sim 6 \times 10^3$, which marks the real onset of the evolution with (pure) magnetic helicity conservation. For a rough estimate of the magnetic field evolution,

however, we shall practically use η_{flip} as the switching time between the adapted Hosking integral conservation and the (pure) magnetic helicity conservation.

H. Cases with initially small $|\mu_{50}|/k_0$

In all the cases considered so far, we assumed $|\mu_{50}|/k_0 > 1$. We now consider the opposite case and discuss runs with $\mu_{50} = -0.1$, keeping still $k_0 = 1$, so $|\mu_{50}|/k_0 = 0.1$ (Runs P, Q, and R), and also a run with $\mu_{50} = -0.5$ and $k_0 = 1$ (Run S). To prevent the magnetic field from being too weak, while still preserving vanishing total chirality, we decrease the value of λ and choose $\lambda = 500, 50$, and 5 for Runs P (and S), Q, and R, respectively. All the runs end at $\eta \sim 10^4$. The parameters of these runs are summarized in Table III. The magnetic diffusivity is taken as $\sigma^{-1} = 2 \times 10^{-4}$. In all our cases, the system does not even reach η_{CPI} . This is because of the small value of $|\mu_{50}|$, which enters the CPI time inverse quadratically; see Eq. (10).

Smaller values of λ correspond to larger magnetic fields. We see that this also leads to a gradual decrease of the scaling index of the envelope of the magnetic energy spectrum, β ; see Fig. 3. For a given value of β , we expect that the scaling indices q , p , and r , for the evolution of the magnetic coherence length ($\xi_M \propto \eta^q$), energy density ($\mathcal{E}_M \propto \eta^{-p}$), and helicity ($\mathcal{H}_M \propto \eta^{-r}$), respectively, are given as $q = 2/(\beta + 3)$, $p = 2(1 - q)$, and $r = p - q$. In Fig. 13(a), we see that for Run P the exponents in agree reasonably well with those expected for $\beta = 1/3$. In Fig. 13(b), we also show the results for Run R, where λ is a hundred times smaller and the magnetic field ten times stronger. Now the value of β is very small (about 0.05), corresponding to $q = 0.66$, $p = 0.69$, and $r = 0.03$. Finally, Fig. 13(c) gives the results for Run S, where $\lambda = 500$ is the same as for Fig. 13(a), but now $\mu_{50} = -0.5$ instead of -0.1 . In this case, similarly to Run P, $\beta \approx 1/3$, $p \approx 4/5$, $q \approx 3/5$, and $r \approx 1/5$.

In Table IV, we list several combinations of the expected scaling indices q , p , and r for $0 \leq \beta \leq 3/2$. Interestingly, in the range $0 \leq \beta \leq 1/3$, the values of q and p do not vary much in this range, especially compared to the case for the evolution with the (adapted) Hosking integral conservation, $\beta = 3/2$, so if they do not agree with those from the simulations, the discrepancy cannot easily be resolved by changing the value of β within reasonable limits. Note that

TABLE III. Empirical values of β for cases with $|\mu_{50}| < k_0$. For a given value of λ , the values of v_{A0} followed from the requirement that the total chirality vanishes. The resulting maximum rms velocity $u_{\text{rms}}^{\text{max}}$ is listed for completeness.

Run	$-\mu_{50}$	λ	v_{μ}	\tilde{v}_{λ}	v_{A0}	$u_{\text{rms}}^{\text{max}}$	SLD	β	η_{I}
P	0.1	500	2×10^{-5}	0.014	0.026	0.008	no	0.33	160
Q	0.1	50	2×10^{-5}	0.045	0.081	0.028	no	0.15	50
R	0.1	5	2×10^{-5}	0.141	0.257	0.076	yes	0.05	27
S	0.5	500	10^{-4}	0.032	0.057	0.019	no	0.33	70

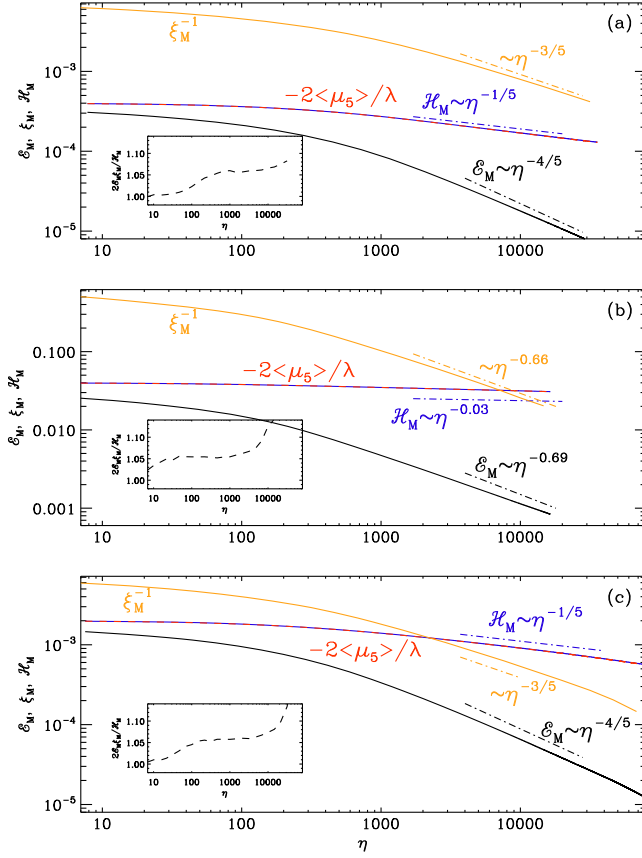


FIG. 13. Time dependence of \mathcal{E}_M (black), ξ_M^{-1} (orange), \mathcal{H}_M (red), and $-2\langle\mu_5\rangle/\lambda$ (blue), for Runs P (a), R (b), and S (c).

$\beta = 0$ is expected if the evolution is governed by (pure) magnetic helicity conservation.

In the corresponding pq diagram Fig. 14, we see that all the runs approach the scale-invariance line $p = 2(1 - q)$. For Run P, it evolves along the line $r = 1/5$. At the intersection, we have $q = 3/5$ and $p = 4/5$. However, for Runs Q and R with stronger magnetic field strengths, expressed in terms of the initial Alfvén speed $v_{A0} = B_0/\sqrt{\rho_0}$ (which is well approximated by \tilde{v}_λ), the solution approaches the $\beta = 0$ line, which suggests better conservation of magnetic helicity. Note that near the end of those runs, the data points may not be reliable because of the finite size of the domain. In addition, because of the stronger magnetic field, the Alfvén time is shorter and

TABLE IV. Possible combinations of $q = 2/(\beta + 3)$, $p = 2(1 - q)$, and $r = p - q$ in the range $0 \leq \beta \leq 1/3$.

β	q	p	r
$3/2 = 1.50$	$4/9 \approx 0.44$	$10/9 \approx 1.11$	$2/3 \approx 0.67$
$1/3 \approx 0.33$	$3/5 = 0.60$	$4/5 = 0.80$	$1/5 = 0.20$
0.15	0.63	0.73	0.10
0.05	0.66	0.69	0.03
0	$2/3 = 0.67$	$2/3 = 0.67$	0

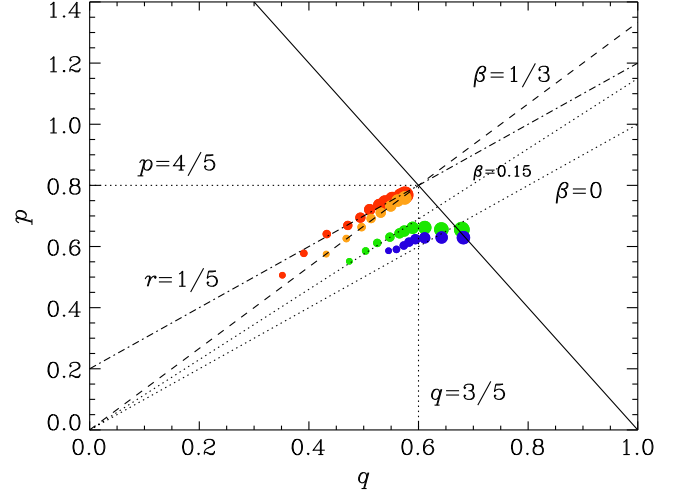


FIG. 14. pq diagram for Runs P (red symbols), S (orange symbols), Q (green symbols), and R (blue symbols) at times $t = 700, 1000, 1500, 2200, 3200, 4600, 6800, 10^4, 1.5 \times 10^4, 2.2 \times 10^4$, and 3.2×10^4 , corresponding to symbols of increasing size. The solid line denotes the scale-invariance line $p = 2(1 - q)$, the dashed line the empirical $\beta = 1/3$ line, and the dashed-dotted line is the resulting $r = 1/5$ line for the magnetic helicity decay. For stronger magnetic field strength (Runs Q and R), the solutions evolve along $\beta \approx 0.15$ and $\beta \approx 0.05$, respectively. Toward the end of the runs, the finite size effects of the domain begin to affect the solution. The dotted line denotes the $\beta = 0$ line for magnetic helicity conservation and is shown for comparison.

therefore k_1 reaches k_1 more quickly. In any case, it is likely that for small $|\mu_{50}|/k_0$, we see a new stage of the evolution of the system where the magnetic helicity and chirality are temporarily conserved individually, as discussed in Sec. II E. This is supported by the fact that the theoretically predicted time of the onset of ACC (or even CPI) should come much later, well after the end of the run; see Eqs. (10) and (31). In other words, from the present simulation results, we cannot distinguish between the two possible theoretical predictions for the later evolution in the case $k_0 > |\mu_{50}|$; see steps 3 or 3' given in Sec. II E.

For all the simulations where initially $|\mu_{50}| < k_0$, we find that μ_5 decays more slowly than k_1 ; see Fig. 15 for Run S, as an example, where we see the crossing of μ_5 and k_1 . The same is also seen for $|\mu_{50}| = 0.1$, but then the crossing of $|\mu_5|$ and k_1 occurs much later and is therefore not yet prominent. Again, these observations suggest that the magnetic helicity-conserving phase is an intermediate one before the solution resumes the decay governed by the adapted Hosking integral, as discussed in Sec. II E.

The time evolution of the magnetic energy and helicity spectra for Run P are given in Fig. 16(a). We can see that a negative magnetic helicity part of the spectrum still emerges, again only at large wave numbers, although now much later. This means that $|\langle\mu_M^- \rangle|$ is induced by the CPI, but it stays extremely small. However, the time is

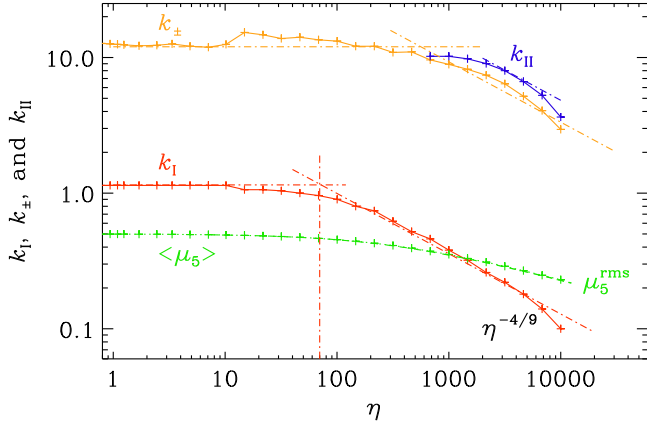


FIG. 15. Comparison of k_I (red), k_{\pm} (orange), and k_{\parallel} (blue) for Run S with $\mu_{50} = -0.5$. The dashed-dotted line indicates $\eta^{-4/9}$. The green dashed line shows $\langle \mu_5 \rangle$ and the green dotted line shows the rms value μ_5^{rms} .

still less than η_{CPI} and hence it is likely that we only see the early stages of the CPI before much stronger amplification is possible. Furthermore, $|\langle \mu_M^+ \rangle|$ does not decay much during the time of the run; see also Fig. 13(b). This can easily be understood by the fact that η_{CPI} is very large in this run. Many other features of the magnetic field evolution

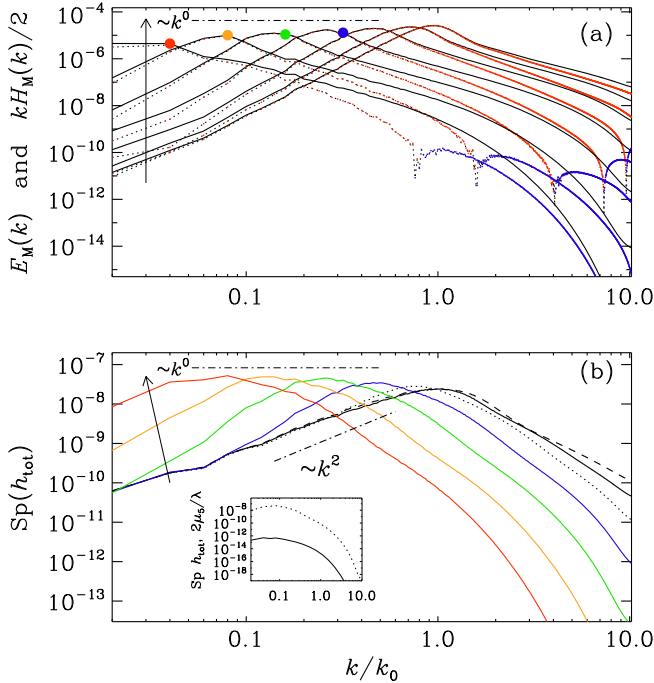


FIG. 16. (a) Magnetic energy and (b) total helicity variance spectra at $t = 70$ (dashed), 200 (solid), 700 (dotted), 2×10^3 (blue), 7×10^3 (green), 2×10^4 (orange), and 7×10^4 (red) for Run S. In (a), note that the $E_M(k, t)$ evolve underneath a $k^{1/3}$ envelope, and the upward arrow indicates the sense of time. In (b), the slopes k^2 , k^4 , and k^{-4} have been indicated and the inset compares $\text{Sp}(2\mu_5/\lambda)$ (solid) with $\text{Sp}(h_{\text{tot}})$ (dotted) at the last time.

remain superficially similar to the limit of large $|\mu_{50}|/k_0$. One still sees inverse cascading of positive magnetic helicity.

I. Nonconservation of $I_H(\eta)$ for small $|\mu_{50}|/k_0$

In Fig. 16(b), we show the total helicity variance spectrum $\text{Sp}(h_{\text{tot}})$. We clearly see that for small k , the value of $\text{Sp}(h_{\text{tot}})$ increases with time. This suggests that the adapted Hosking integral, as defined in Ref. [55], is not conserved at late times.

In Fig. 17, we show for Run S the Hosking integral, I_H , as a function of time. It is obtained from the function $\mathcal{I}_H(R, \eta) = L^{-3} \int w(\mathbf{k}, R) \text{Sp}(h_{\text{tot}}) d^3\mathbf{k} / (2\pi)^3$, which is shown in the inset as a function of R at different times. Here, $w(k, R) = (4\pi R^3/3)[6j_1(kR)/kR]^2$ is a weight function [58] with j_n being spherical Bessel functions. The relevant value of R is usually where R is just a little less than half the system size [56,58], which is here for $k_0 R = 50\pi \approx 157$. At that location, $\mathcal{I}_H(R, \eta)$ usually also shows an approximate plateau for different times. This is not the case for this run. We have therefore chosen instead the value $k_0 R = 30$, which is where $\mathcal{I}_H(R, \eta)$ shows considerable spread in time. This position is marked in the inset by the vertical dashed line. Focusing now on the resulting time dependence of $I_H(\eta)$, we see a sharp rise at late times ($\eta \geq 10^4$), which also agrees with the time when we saw the values of $\text{Sp}(h_{\text{tot}})$ for small k to change; see Fig. 16(b).

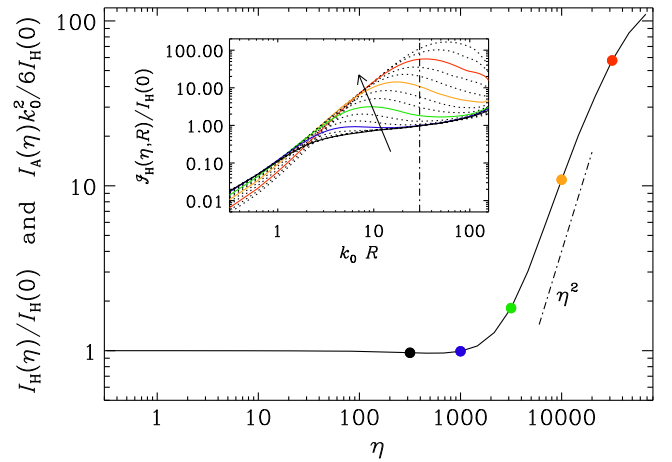


FIG. 17. $I_H(t)$, normalized by its initial value, for Run P. The inset shows $\mathcal{I}_H(R, t)$ versus R at different times: solid lines correspond to $\eta = 320$, 1000 , 3200 , $10,000$, and $32,000$ are in black, blue, green, orange, and red, respectively. The dotted lines mark intermediate times. The colors of the symbols in the graph of $I_H(t)$ correspond to those of the lines in the inset, and also to those in Fig. 16. The adapted Hosking integral is evaluated as $I_H(t) = \mathcal{I}_H(R_*, t)$. The vertical dashed-dotted line marks the value $k_0 R_* = 100$, which is where the curves show a plateau at early times.

Regarding the conserved quantity for runs in the limit of small $|\mu_{50}|/k_0$, we can say that, in spite of vanishing total chirality, the Hosking integral is here not conserved, because the magnetic energy now peaks at scales where the CME is not effective during the time of the run and the magnetic helicity is conserved. As a result, the net chirality is no longer random, but systematically of positive sign. The subinertial range of the magnetic helicity variance begins to be dominated by a k^4 spectrum, which suggests that the Hosking integral in the expansion $\text{Sp}(h_{\text{tot}}) = I_{\text{H}}k^2/2\pi^2 + O(k^4)$ is now subdominant.

To summarize, these runs are consistent with the theoretical prediction in Sec. II E, up to the intermediate stage (step 2), although a moderate violation of helicity conservation has been seen for Run P. Note that Run P has a larger value of λ , which makes the theoretically predicted η_{ACC} smaller [see Eq. (31)], so that an earlier transition to the evolution with adapted Hosking integral conservation is expected. For an analytic estimate of the evolution of the system in the next section, we shall use the theoretical prediction discussed in Sec. II E. Namely, the system is frozen until $\eta = \eta_\lambda$ and then evolves with the usual inverse cascade for the helical magnetic field as an intermediate stage. We chose step 3' for the onset of the ACC, which is more realistic, though at present we do not have any support from numerical results. That is, at $\eta = \eta_{5\text{dec}}$ the system starts to evolve with a decay law determined by the conservation of the adapted Hosking integral.

IV. APPLICATION TO THE EARLY UNIVERSE

A. From QED to the Standard Model

Now we investigate the impact of our findings in the previous sections on the cosmology of the early Universe, especially baryogenesis. Up to here, we focused on a QED-like theory. Thus, we first would like to clarify its relation to the dynamics in the early Universe. The SM involves the right-handed leptons e_{Rf} , the left-handed lepton doublets ℓ_{Lf} , the right-handed up- and down-type quarks, u_{Rf} and d_{Rf} , and the left-handed quark doublets q_{Lf} with the flavor index running through $f = 1, 2, 3$, alongside the scalar Higgs doublet Φ , which are in total 16 species. On top of this, we have gauge interactions of $U(1)_Y \times SU(2)_L \times SU(3)_C$. It is not obvious why we can reduce this complicated system to chiral MHD based on a QED-like theory like the one introduced in Sec. II.

What we are interested in here is the slow dynamics at long wave lengths compared to interactions among particles. The key idea for the reduction is to assume the equilibration of fast interactions and to keep only the slow variables. The hypermagnetic field of $U(1)_Y$ with a correlation length much larger than the mean free path of the particles stands out as a slow variable because the magnetic flux cannot be cut thanks to the absence of monopoles. This feature does not hold for non-Abelian

gauge fields because they are charged under their own gauge group. We also need the chiral chemical potential, since it is related to the magnetic field via the anomaly equation. Apart from these two fundamental building blocks, we can coarse-grain the microscopic properties of all particle in the form of transport coefficients such as the diffusion constant and the electric conductivity, besides macroscopic quantities such as the pressure, energy density, and velocity field. In this way, one may see that the system can be reduced to chiral MHD as far as the slow and long-wave dynamics is concerned.

Still, one might wonder why we can just focus on one particular chiral chemical potential, as in Eq. (3), since we have 15 chiral fermion species in the SM. To illustrate this, let us focus on the temperature right above 10^5 GeV, where the electron Yukawa interaction is not efficient compared to the cosmic expansion, but other interactions are fast enough. In this case, the chiral chemical potential for the right-handed electron, $\tilde{\mu}_e$, should be counted as a slow variable, as it is directly related to the hypermagnetic field via the anomaly equation. On the other hand, other chiral chemical potentials are subject to fast SM interactions, which provides 11 nontrivial constraints among them. Recalling that the SM has four conserved charges, hypercharge Y and the flavored baryon-minus-lepton numbers $B/3 - L_f$ with $f = 1, 2, 3$, one may immediately see that the remaining 15 chemical potentials can be expressed as a function of $\tilde{\mu}_e$ by solving $11 + 4$ constraints. The chiral chemical potential $\tilde{\mu}_5$ originates from the generalized Ohm's law,

$$\mathbf{J}_Y = \sigma_Y \mathbf{E}_Y + \frac{2\alpha_Y}{\pi} \tilde{\mu}_5 \mathbf{B}_Y, \quad (39)$$

where α_Y is now the $U(1)_Y$ fine-structure constant and σ_Y the hyperelectric conductivity of the plasma. In the following, we will work with the α_Y value around the electroweak scale, $\alpha_Y \simeq 0.01$, and neglect its renormalization group running when considering the dynamics of the hypermagnetic field at high energies. Also, note that, in this section, we set $\hbar = c = k_B = 1$, and all quantities are physical rather than comoving, unless explicitly stated otherwise. For the SM $U(1)_Y$, at $T \sim 10^{5\cdots 6}$ GeV, one may express this $\tilde{\mu}_5$ as a summation of chiral chemical potentials for the SM fermions as [12,49]

$$\tilde{\mu}_5 = \sum_{i=1}^{15} \epsilon_i g_i y_i^2 \frac{\tilde{\mu}_i}{2} = \frac{711}{481} \frac{\tilde{\mu}_e}{2}, \quad (40)$$

where i runs over all SM fermions, $\epsilon_i = \pm$ for right- and left-handed fermions, respectively, g_i counts internal degrees of freedom, and y_i is the hypercharge of fermion species i . In the second equality, we inserted the solution of the 15 constraint equations mentioned above. We now see that, up to the $\mathcal{O}(1)$ coefficient of $711/481$, one chiral

chemical potential suffices to describe the system. In higher temperature regimes, we will have additionally more slow variables that enter the expression of $\tilde{\mu}_5$, but it is still written as a linear combination of their chemical potentials with $\mathcal{O}(1)$ coefficients. It still holds that the evolution of the system is described by chiral MHD as discussed in Sec. II with $\tilde{\mu}_5$ being evaluated accordingly.

B. Baryogenesis

After these general remarks, let us now turn to the implications of our analysis for the generation of the baryon asymmetry of the Universe. We are primarily interested in the scenario of baryogenesis from decaying hypermagnetic helicity [19,20,24–26], which assumes the presence of a strongly helical hypermagnetic field during the radiation-dominated era in the early Universe. This scenario is based on the observation that the helicity stored in the hypermagnetic field decays at the time of the electroweak phase transition, not because of some exotic helicity-violating interactions, but simply because hypermagnetic helicity is converted to magnetic helicity. This decay of hypermagnetic helicity then sources a baryon asymmetry via the chiral anomaly of the baryon-number current.

One possibility to generate the helical hypermagnetic field required for baryogenesis consists of axion inflation featuring a Chern–Simons coupling to $U(1)_Y$. Such a model leads to the nonperturbative production of hypermagnetic gauge fields in combination with charge asymmetries for the 15 chiral SM fermion species [48,49],

$$n_i - \bar{n}_i = \frac{1}{6} g_i \tilde{\mu}_i T^2 = -\epsilon_i g_i y_i^2 \frac{\alpha_Y}{2\pi} h_Y + \dots, \quad (41)$$

where the ellipsis represents all other SM contributions, which, however, can safely be neglected during inflation.⁴ Furthermore, h_Y in Eq. (41) is the physical helicity density, which we define in terms of the comoving vector potential $\mathbf{A}_{Y,\text{com}}$, comoving hypermagnetic field $\mathbf{B}_{Y,\text{com}}$, and scale factor a ,

$$h_Y = \frac{1}{a^3} \langle \mathbf{A}_{Y,\text{com}} \cdot \mathbf{B}_{Y,\text{com}} \rangle, \quad (42)$$

where the angle brackets now stand for a double average including the spatial average and the quantum mechanical expectation value during inflation. From Eq. (41), we can read off the fermion chemical potentials at the end of inflation in terms of the helicity density at the end of inflation. Inserting this result into Eq. (40), we obtain the chiral chemical potential at the end of inflation,

⁴The top-quark Yukawa interaction would be a possible exception; see the discussion in footnote 5 of Ref. [49] for more details.

$$\frac{\tilde{\mu}_5}{T} = -\frac{c_5}{2} 6\chi, \quad c_5 = \frac{95}{18}, \quad (43)$$

where the dimensionless yield parameter χ quantifies the amount of CP violation during axion inflation [49],

$$\chi = \frac{\alpha_Y h_Y}{2\pi T^3}. \quad (44)$$

Here, we assume instantaneous reheating. The same coefficient c_5 was found in Ref. [49]; in total, the expression for $\tilde{\mu}_5$ in Eq. (43) is, however, smaller than the one in Ref. [49] by a factor of 1/2 because, in the present paper, we include a factor of 1/2 in Eq. (40).

The fermion asymmetries generated during axion inflation are consistent with the chiral anomalies of the respective fermion currents. In fact, it is straightforward to generalize the conversion law in Eq. (8) to the early Universe. To see this, let us rewrite Eq. (43) as follows:

$$\mu_5 + \frac{3c_5}{2} \left(\frac{2\alpha_Y}{\pi} \right)^2 \frac{1}{2a^3 T^2} \langle \mathbf{A}_{Y,\text{com}} \cdot \mathbf{B}_{Y,\text{com}} \rangle = 0, \quad (45)$$

where we used $\mu_5 = (2\alpha_Y/\pi)\tilde{\mu}_5$. Then, introducing

$$\lambda_Y = 3 \left(\frac{2\alpha_Y}{\pi a T} \right)^2, \quad (46)$$

we obtain the relation

$$\mu_5 + \frac{c_5}{2} \mu_M^Y = 0, \quad (47)$$

where

$$\mu_M^Y = \frac{1}{2a} \lambda_Y \langle \mathbf{A}_{Y,\text{com}} \cdot \mathbf{B}_{Y,\text{com}} \rangle. \quad (48)$$

As the temperature in the early Universe decreases, more and more SM interactions reach chemical equilibrium. This includes the SM Yukawa interactions, which violate parity and hence render the coefficient c_5 in Eq. (43) a time-dependent quantity [49]. During axion inflation, c_5 assumes its maximal value, $c_5 = 95/18 \simeq 5.3$, before it then decreases down to $c_5 = 711/481 \simeq 1.5$ at temperatures of a few 100 TeV [see Eq. (40)]. This change in c_5 is reflected in a changing value of the chiral chemical potential μ_5 , which is always given by $\mu_5 = -c_5/2\mu_M^Y$ according to Eq. (47), with μ_M^Y remaining constant until the onset of CPI, ACC, or electroweak phase transition. At $T \lesssim 10^5$ GeV, c_5 and hence μ_5 vanish because all SM interactions have reached chemical equilibrium.

The CP asymmetry parameter χ in Eq. (44) controls the outcome of baryogenesis from helicity decay. That is, if no CPI or ACC takes place before the onset of spin flipping, the decay of hypermagnetic helicity around the electroweak

phase transition results in a present-day baryon asymmetry (quantified in terms of the baryon-to-photon ratio) that is fully controlled by χ [49],

$$\eta_B^0 \equiv \frac{n_B^0}{n_\gamma} \simeq 0.15 c_B^{\text{dec}} \chi, \quad (49)$$

where $n_\gamma = 2\zeta(3)T^3/\pi^2$ and the superscript 0 indicates that a quantity is evaluated at the present time. Here, the coefficient c_B^{dec} has a theoretical uncertainty of possibly two orders of magnitude [26]. In the following, we will work with the representative value $c_B^{\text{dec}} = 0.05$ [49,50], which implies that χ values of the order of $\chi \sim 10^{-7}$ are necessary to reproduce the observed baryon asymmetry, $\eta_B^{\text{obs}} \simeq 6.1 \times 10^{-10}$ [75,76]. Meanwhile, the parameter χ also allows us to evaluate the ratio of k_0 and μ_5 at the end of axion inflation. Specifically, if we estimate the comoving peak wave number k_0 in terms of the comoving wave number that enters the Hubble horizon at the end of reheating, $k_{\text{rh}} = a_{\text{rh}} H_{\text{rh}}$ [49], we find

$$\begin{aligned} \frac{|\mu_5|}{k_{\text{rh}}/a_{\text{rh}}} &= \frac{6\alpha_Y c_5 \chi}{\pi} \frac{T_{\text{rh}}}{H_{\text{rh}}} = \frac{6\alpha_Y c_5 \chi M_*}{\pi T_{\text{rh}}} \\ &\sim 10^{-4} \left(\frac{\chi}{10^{-7}} \right) \left(\frac{10^{14} \text{ GeV}}{T_{\text{rh}}} \right), \end{aligned} \quad (50)$$

where $M_* = (90/\pi^2/g_*)^{1/2} M_{\text{Pl}} \simeq 7.1 \times 10^{17}$ GeV is the reduced Planck mass, $M_{\text{Pl}} \simeq 2.4 \times 10^{18}$ GeV, rescaled by the effective number of relativistic degrees of freedom in the Standard Model plasma, $g_* = 427/4$. Axion inflation typically results in small values of the χ parameter (e.g., $\chi \sim 10^{-7}$; see above) and large values of the reheating temperature (e.g., $T_{\text{rh}} \sim 10^{14}$ GeV; see Ref. [49]), which puts us in the parametric regime where $|\mu_5| \ll k_{\text{rh}}/a_{\text{rh}}$ at the end of axion inflation. Moreover, smaller values of T_{rh} typically result in smaller values of χ , following the scaling relation $\chi \propto (T_{\text{rh}}/M_*)^3$ [49], which means that the opposite hierarchy, $|\mu_5| \gg k_{\text{rh}}/a_{\text{rh}}$, cannot simply be obtained by considering a smaller reheating temperature.

For $|\mu_5| \ll k_{\text{rh}}/a_{\text{rh}}$, the chiral chemical potential eventually becomes larger than the peak wave number of the hypermagnetic energy spectrum. This is because the peak momentum decreases via the inverse cascade, while the chiral chemical potential is approximately conserved. As mentioned above Eq. (34), we expect a large hierarchy between μ_5 and k_1 at η_{CPI} for the SM plasma,

$$\frac{|\mu_5|}{k_1/a_{\text{CPI}}} \simeq \left(\frac{2\sigma_Y^2}{\bar{\rho}\lambda_Y} \right)^{1/3} \quad (51)$$

$$\sim 2 \times 10^2 \left(\frac{106.75}{g_*} \right)^{1/3} \left(\frac{0.01}{\alpha_Y} \right)^{2/3}, \quad (52)$$

where we evaluate the hyperelectric conductivity σ_Y as $\sigma_Y = c_{\sigma_Y} T$, with $c_{\sigma_Y} \sim 10^2$ [72,73], the average radiation

energy density $\bar{\rho}$ as $\bar{\rho} = c_{\bar{\rho}} T^4$, with $c_{\bar{\rho}} = \pi^2 g_*/30$, and the parameter λ_Y as $\lambda_Y = c_{\lambda_Y}/(aT)^2$ with $c_{\lambda_Y} = 12\alpha_Y^2/\pi^2$. The net chiral chemical potential may start to decay after some duration of CPI as given in Eq. (34)

$$\eta_{5\text{dec}} = c_A \eta_{\text{CPI}} = c_A \left[\frac{1 \sigma_Y}{a \mu_5^2} \right]_{\text{rh}}, \quad (53)$$

where the factor of a^{-1} follows from the mass dimension of the factor σ_Y/μ_5^2 .

The time $\eta_{5\text{dec}}$ marks the onset of the net chirality decay via the CPI and needs to be compared to the time $\eta_{\text{sf}} = 1/k_{\text{sf}}$ when spin flipping for left- and right-handed electrons becomes efficient, where $k_{\text{sf}} = a_{\text{sf}} H_{\text{sf}}$ is the comoving horizon scale at $\eta = \eta_{\text{sf}}$. Using Eq. (53), together with $T_{\text{sf}} = 10^5$ GeV for the electron Yukawa interaction in the SM [45,46], we obtain

$$\frac{\eta_{5\text{dec}}}{\eta_{\text{sf}}} \sim \left(\frac{g_*}{106.75} \right)^{1/2} \left(\frac{0.01}{\alpha} \right)^2 \left(\frac{c_A}{10} \right) \left(\frac{10^{-4}}{\chi} \right)^2. \quad (54)$$

If chirality decay occurs before the onset of spin flipping, i.e., $\chi \gtrsim 10^{-4}$, we expect the hypermagnetic helicity to decay simultaneously. Therefore, the correct amount of baryon asymmetry would be obtained for such a large $\chi \gg 10^{-7}$ that would overproduce baryon (49) at a first glance, since the reduction of the hypermagnetic helicity because of the CPI might counteract this overproduction of baryon number. To see this explicitly, one may use the ratio in Eq. (54) to introduce a dilution factor, $\Delta = (\eta_{5\text{dec}}/\eta_{\text{sf}})^{q_5}$ with q_5 being the scaling index introduced in Eq. (35), that multiplies the naive baryon asymmetry in Eq. (49) whenever the CPI should occur before the onset of spin flipping,

$$\eta_B^0 \simeq \min \{1, \Delta\} \times 0.15 c_B^{\text{dec}} \chi. \quad (55)$$

By requiring $\eta_B^0 \simeq 6.1 \times 10^{-10}$, we can estimate the size of the CP violation χ required to obtain the observed baryon-to-photon ratio. For $q_5 = 2/3$, we need $\chi \sim 10^6$. Such large χ values are extremely difficult, if not impossible, to realize in realistic models of axion inflation. For $q_5 = 4/3$, we need instead $\chi \sim 10^{-2}$, which is still large but not an unrealistic value for axion inflation. In this way, the result for the final baryon asymmetry strongly depends on the scaling index q_5 , whose precise value is, however, beyond the scope of our current simulations.

To sum up, even if we initially start from $|\mu_5| \ll k_{\text{rh}}/a_{\text{rh}}$, the system eventually ends up with the large hierarchy of $|\mu_5| \gg k_1/a$. Moreover, if χ is extremely large, we can have initially $|\mu_5| \gg k_1/a$. These cases might display similar dynamics as our Runs III–VI, which we commented on at

the end of Sec. III D. The decay law for the magnetic helicity may then be different from the $\eta^{-2/3}$ behavior that we typically find for ACC, which strongly affects the outcome of baryogenesis. As already stated in Sec. III D, we leave a more detailed study of this more exceptional case for future work.

V. CONCLUSIONS

We have performed numerical simulations of chiral MHD with zero initial total chirality for a range of parameters to determine the dependence of characteristic time and scale ratios, which are well explained by the analytical estimate in Sec. II E. Namely, they are consistent with the scaling evolution, $\xi_M \propto \eta^{4/9}$, $\mathcal{E}_M \propto \eta^{-10/9}$, and $\langle \mu_5 \rangle \propto \eta^{-2/3}$, derived from the conservation of the adapted Hosking integral [55], and also the timescale of the onset of this scaling evolution, η_{ACC} ; see Eqs. (26) and (31). Our numerical simulations also assess the possibility of artifacts resulting from insufficient scale separation. A particularly important constraint is a sufficiently large size of the computational domain (small k_1), which is needed to obtain the expected $\eta^{4/9}$ scaling of the correlation length. When this constraint is not obeyed, the scaling is closer to $\eta^{1/3}$. The second constraint of a sufficiently large Nyquist wave number is important to obtain the correct values of the scale ratio of the positive and negative magnetic helicity peaks, i.e., $k_{\text{II}}/k_{\text{I}}$. Somewhat surprisingly, this ratio scales inversely with the initial scale separation between the scale of the magnetic field and the CPI scale. Increased values of $\langle \mu_{\text{M}}^- \rangle$, which characterize the strength of the CPI, are obtained when σ is small or $|\mu_{50}|$ is large and therefore the coupling to the CPI is more efficient.

In the absence of spin flipping, even the slightest initial imbalance will amplify as the magnetic energy decays; see Appendix C. On long timescales, this eventually leads to a fully helical state, although simulations of this are at present unable to demonstrate this conclusively owing to the finite size of the computational domain. Spin flipping is another mechanism that can produce an imbalance between magnetic helicity and fermion chirality. In any case, however, the finally available magnetic energy and helicity densities are always limited by the finiteness of the initial total chirality imbalance. For $\eta < \eta_{\text{ACC}}$, when the chiral magnetic effect is not effective at the peak-scale, magnetic helicity conservation governs the decay of magnetic energy and the Hosking integral does not play a role.

We also discussed the implications of our findings for the generation of the baryon asymmetry of the Universe, in particular, the scenario of baryogenesis from helicity decay. The final baryon asymmetry in this scenario is controlled by a dimensionless yield parameter χ that quantifies the helicity density produced in the very early Universe, for instance, during a stage of axion inflation. In previous

work, it was shown how the observed baryon asymmetry can be generated from helicity decay at the time of the electroweak phase transition for a specific χ value, $\chi_0 \sim 10^{-7}$; see Eq. (49) and Ref. [49]. The situation at larger χ values, however, remained unclear. At $\chi \gg 1$, one may have anticipated either (A) the overproduction of baryon number or (B) catastrophic helicity erasure by the chiral plasma instability and consequently no baryon asymmetry at all.

Thanks to the analysis in this paper, we now extend the previous analysis to the case where the decay of the hypermagnetic helicity occurs before the spin flipping for electrons becomes efficient, i.e., $\chi \gtrsim 10^{-4}$. For typical parameters for axion inflation, although we initially have $|\mu_5| \ll k_{\text{rh}}/a_{\text{rh}}$, the opposite large hierarchy is eventually realized $|\mu_5| \gg k_{\text{I}}/a_{\text{I}}$. Therefore the required value of χ to reproduce the observed baryon asymmetry depends on the value of the scaling index q_5 in the large hierarchy regime. Further studies for the large hierarchy are indispensable for understanding the outcome of baryogenesis.

The source code used for the simulations of this study, the `PENCIL CODE`, is freely available from Ref. [67]. The simulation setups and the corresponding data are freely available from Ref. [77].

ACKNOWLEDGMENTS

We thank V. Domcke for fruitful discussions and J. Warnecke for his work on the implementation of SLD, which is used in some of the simulations. We are also indebted to the referee for valuable suggestions. Support through Grant No. 2019-04234 from the Swedish Research Council (Vetenskapsrådet) and NASA ATP Award No. 80NSSC22K0825 (AB), Grant-in-Aid for Scientific Research No. (C) JP19K03842 from the JSPS KAKENHI (K. K.), MEXT Leading Initiative for Excellent Young Researchers No. JPMXS0320200430 (K. M.), Grant-in-Aid for Young Scientists No. JP22K14044 from the JSPS KAKENHI (K. M.), and Grant No. 185863 from the Swiss National Science Foundation (J. S.) are gratefully acknowledged. We acknowledge the allocation of computing resources provided by the Swedish National Infrastructure for Computing (SNIC) at the PDC Center for High Performance Computing Stockholm and Linköping.

APPENDIX A: ADDITIONAL TIME AND LENGTH SCALES

In Sec. II E and also later in this paper, we defined a number of timescales and wave numbers. In Table I, we summarized the characteristic time scales relevant for the evolution of the system. In Table V we present a summary of additional timescales and in Table VI various wave numbers defined in this paper.

TABLE V. Summary of additional timescales used in this paper and not yet defined in Table I.

Timescale	Definition	Explanation
η_{flip}	Sec. II C, Eq. (21)	Time when spin flipping is turned on
η_{off}	Sec. II C, Eq. (21)	Time when spin flipping is later turned off again
η_0	Sec. II D	Initial time
$\eta_{5\text{dec}}$	Sec. II E, Eqs. (34) and (53)	Time when decay is determined by conservation of adapted Hosking integral
η_{I}	Sec. III B	Time when large-scale spectrum starts to decrease via inverse cascade
$\eta_{\pm}^{(i)}$	Sec. III B	Time when negative helicity modes at secondary peak starts to decrease
$\eta_{\pm}^{(ii)}$	Sec. III B	Time when decay of the secondary peak becomes slower with a smaller index
$\eta_{\mu_{\text{M}}^+}$	Sec. III D	Time when the ACC commences exhibiting a power law decay
$\eta_{\mu_{\text{M}}^-}$	Sec. III D	Time when the ACC decays again
η_{B}^0	Sec. IV B, Eqs. (49) and (55)	Theoretical time when present-day baryon asymmetry is established
$\eta_{\text{B}}^{\text{obs}}$	Sec. IV B	Observed time when present-day baryon asymmetry is established
η_{sf}	Sec. IV B	Spin flipping time

TABLE VI. Summary of wave numbers defined in this paper.

Wave number	Definition	Explanation
k_{p}	Sec. I	Equivalent to ξ_{M}^{-1} , i.e., the time-dependent peak wave number of $E_{\text{M}}(k)$
k_{I}	Sec. II B	Lowest wave number in the domain = $2\pi/L$
k_{Ny}	Sec. II B	Nyquist wave number = $N\pi/L$
k_0	Sec. II C, Eq. (22)	Wave number of the initial peak of $E_{\text{M}}(k)$
k_{I}	Sec. II C	Peak wave number of the positive peak of $H_{\text{M}}(k)$
k_{II}	Sec. II C	Peak wave number of the negative peak of $H_{\text{M}}(k)$
k_{\pm}	Sec. II C	Wave number where $H_{\text{M}}(k)$ changes sign
μ_{50}	Sec. II C	Initial value of μ_5 , critical CPI wave number
k_{th}	Sec. IV B	Wave number of the Hubble horizon at end of reheating
k_{sf}	Sec. IV B	Inverse spin flipping time, i.e., $1/\eta_{\text{sf}}$

APPENDIX B: OTHER CASES WITH SPIN FLIPPING

In Sec. III G, we presented Run F with spin flipping, whose other parameters were similar to those of Runs N and N', where $\eta_{\text{ACC}} \approx (\eta_{\text{CPI}}\eta_{\text{diff}})^{1/2} = 10^3$. and $|\mu_{50}|/k_0 = 5$. We now discuss a spin flipping version of Run VI (Run P), where $\eta_{\text{ACC}} = 13$ (5×10^4) is much less (much greater) than the spin-flipping time, and where $|\mu_{50}|/k_0 = 160$ ($|\mu_{50}|/k_0 = 0.1$) is much larger (smaller) than for Run F. The results are shown in Figs. 18(a) and 18(b).

As expected, when chirality flipping becomes effective much before the onset of ACC, we hardly see its effect; see Fig. 18(a). Conversely, when mild ACC has already started by the time the chirality flipping becomes effective, we do not see qualitative differences to the original Run P; see Fig. 18(b). Hence, the overall understanding of the effect of chirality flipping does not change, and the

basic features of chirality flipping are best captured in Fig. 11.

APPENDIX C: BEHAVIOR IN IMBALANCED CHIRALITY DECAY

In Sec. V, we emphasized that even the slightest initial imbalance between magnetic helicity and fermion chirality will amplify as the magnetic energy decays. It is therefore important to remember that the dynamics discussed in this paper is specific to the case of balanced chirality, which is arguably also the most generic case. We know that the decay of magnetic energy and the increase of the correlation length follow a different behavior in the completely imbalanced case compared to the unbalanced one. We now discuss the behavior for the mildly imbalanced case. Here, we show that there is a tendency for the system to approach the behavior of a completely imbalanced one.

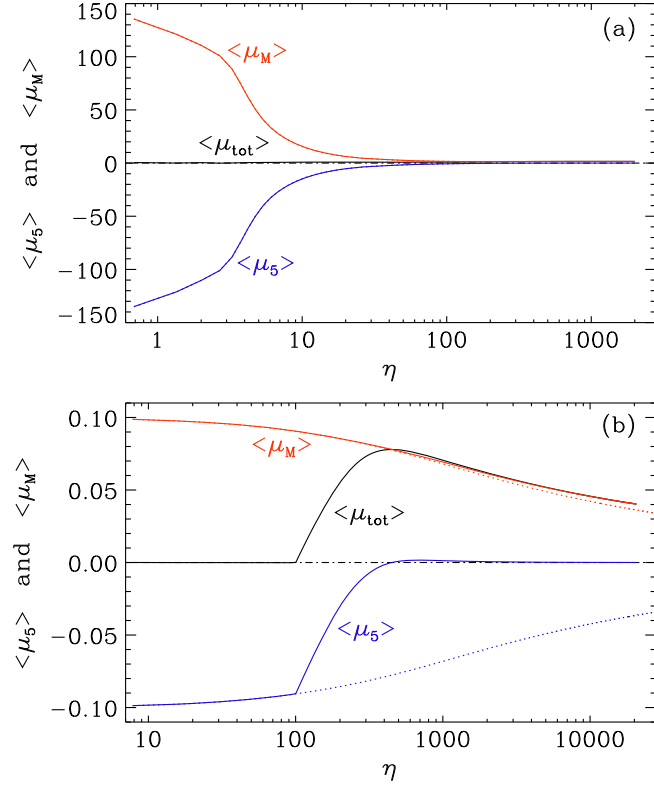


FIG. 18. Similar to Fig. 11, but with parameters similar to Run VI (a) and Run P (b), where $\eta_{\text{ACC}} \approx 13$ is much less than η_{flip} and $\eta_{\text{ACC}} \approx 5 \times 10^4$ is much greater than η_{flip} . As for Run F in Fig. 11, we have $\eta_{\text{flip}} = 100$ also here for both runs, but do not consider finite values of η_{off} .

We discuss two runs, Run A where the initial $\langle \mu_M \rangle$ is enhanced by 20% compared with $|\langle \mu_5 \rangle|$, and Run B where it is decreased by 20%. Apart from that, the runs are the same as Run O, i.e., the run discussed in Ref. [55].

In Run A, where the magnetic helicity is weaker than in Run O, the CPI becomes dominant and overcompensates

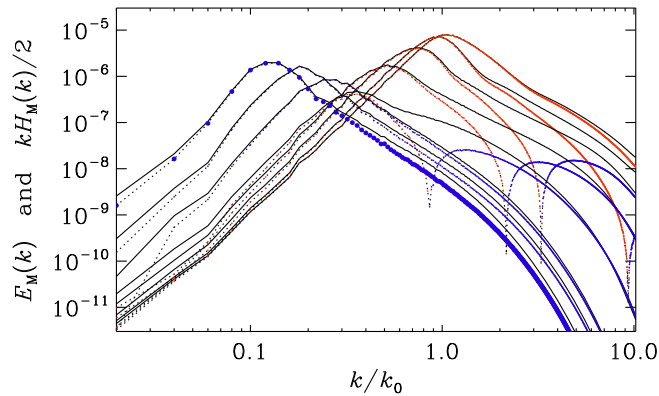


FIG. 19. Magnetic energy (solid lines) and normalized helicity spectra $kH_M(k)/2$ (dotted lines with red and blue symbols for positive and negative helicity spectra, respectively) for Run A at times $\eta = 32, 100, 320, 1000, 3200, 15,000, 22,000,$ and $32,000$.

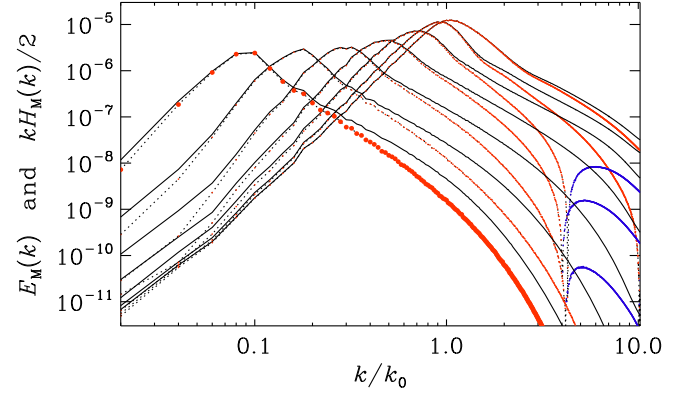


FIG. 20. Same as Fig. 3, but for Run B at times $\eta = 32, 100, 320, 1000, 3200, 10,000,$ and $32,000$.

the magnetic helicity. The net chirality is then negative. Eventually, the sign of the magnetic helicity changes and all the remaining fermion chirality is converted to magnetic fields with negative helicity; see Fig. 19, where we show the magnetic energy $\mathcal{E}_M(k, t)$ and the normalized magnetic helicity spectra $kH_M(k)/2$ for Run A at times $\eta = 32, 320, 1000, 3200, 10,000,$ and $32,000$. We see that $|kH_M(k)|/2$ approaches $\mathcal{E}_M(k)$ near the maximum. In view of the spectral realizability condition, Eq. (16), this means that

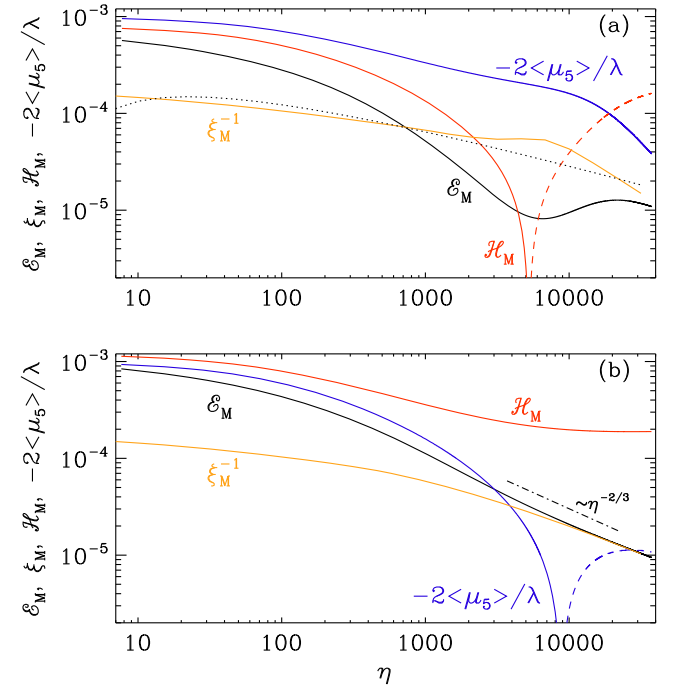


FIG. 21. Time dependence of \mathcal{E}_M (black), ξ_M^{-1} (orange), \mathcal{H}_M (red), and $-2\langle \mu_5 \rangle / \lambda$ (blue), for (a) Run A with smaller and (b) Run B with larger magnetic helicity than in the balanced case. Dashed lines indicate negative values; at late times $-2\langle \mu_5 \rangle / \lambda$ changes sign in (a), and \mathcal{H}_M changes sign in (b). In (a) the dotted line denotes the $\eta^{-1/2} \log(\eta/\eta_{\text{log}})$ scaling of Ref. [15] with $\eta_{\text{log}} = 3$.

the magnetic field is fully helical. Away from the maxima, the inequality is no longer saturated, but this is a typical effect in all turbulent flows where the current helicity spectrum shows a Kolmogorov-type spectrum, making the magnetic helicity spectrum therefore steeper than what could still be allowed by the spectral realizability condition [78].

On the other hand, when the fermion chirality is weak (Run B), the usual inverse magnetic cascade quickly gets established; see Fig. 20. In either case, the fermion chirality gets ultimately converted into magnetic helicity. It just takes a little longer than when the magnetic helicity is initially weak. At the end, however, the usual inverse cascade for a fully helical magnetic field commences. The

sign of magnetic helicity can be positive or negative, depending on the sign of the initial total chirality.

To illustrate how the decay laws change when magnetic helicity and fermion chirality no longer balance, we plot in Fig. 21 the time dependencies of \mathcal{E}_M , ξ_M , \mathcal{H}_M , and $-2\langle\mu_5\rangle/\lambda$, for (a) Run A with 20% smaller and (b) Run B with 20% larger magnetic helicity than in the balanced case. In both cases, we see a tendency of the decays of \mathcal{E}_M and ξ_M^{-1} to slow down while those of \mathcal{H}_M and $-2\langle\mu_5\rangle/\lambda$ follow separate evolutions. Especially in the case of Run B, where the magnetic helicity dominates of the fermion chirality, we see a tendency toward a $\mathcal{E}_M \propto \xi^{-1} \propto t^{-2/3}$ as well as $\mathcal{H}_M = \text{const}$ evolution, as expected from magnetic helicity conservation.

-
- [1] D. T. Son and P. Surowka, Hydrodynamics with Triangle Anomalies, *Phys. Rev. Lett.* **103**, 191601 (2009).
 - [2] Y. Neiman and Y. Oz, Relativistic hydrodynamics with general anomalous charges, *J. High Energy Phys.* **03** (2011) 023.
 - [3] A. Boyarsky, J. Fröhlich, and O. Ruchayskiy, Self-Consistent Evolution of Magnetic Fields and Chiral Asymmetry in the Early Universe, *Phys. Rev. Lett.* **108**, 031301 (2012).
 - [4] A. Boyarsky, J. Fröhlich, and O. Ruchayskiy, Magnetohydrodynamics of chiral relativistic fluids, *Phys. Rev. D* **92**, 043004 (2015).
 - [5] P. Pavlović, N. Leite, and G. Sigl, Chiral magnetohydrodynamic turbulence, *Phys. Rev. D* **96**, 023504 (2017).
 - [6] I. Rogachevskii, O. Ruchayskiy, A. Boyarsky, J. Fröhlich, N. Kleeorin, A. Brandenburg, and J. Schober, Laminar and Turbulent dynamos in chiral magnetohydrodynamics. I. theory, *Astrophys. J.* **846**, 153 (2017).
 - [7] A. Brandenburg, J. Schober, I. Rogachevskii, T. Kahniashvili, A. Boyarsky, J. Fröhlich, O. Ruchayskiy, and N. Kleeorin, The turbulent chiral magnetic cascade in the early universe, *Astrophys. J.* **845**, L21 (2017).
 - [8] J. Schober, I. Rogachevskii, A. Brandenburg, A. Boyarsky, J. Fröhlich, O. Ruchayskiy, and N. Kleeorin, Laminar and turbulent dynamos in chiral magnetohydrodynamics. II. simulations, *Astrophys. J.* **858**, 124 (2018).
 - [9] L. Del Zanna and N. Bucciantini, Covariant and 3+1 equations for dynamo-chiral general relativistic magnetohydrodynamics, *Mon. Not. R. Astron. Soc.* **479**, 657 (2018).
 - [10] S. L. Adler, Axial vector vertex in spinor electrodynamics, *Phys. Rev.* **177**, 2426 (1969).
 - [11] J. S. Bell and R. Jackiw, A PCAC puzzle: $\pi^0 \rightarrow \gamma\gamma$ in the σ model, *Nuovo Cimento A* **60**, 47 (1969).
 - [12] M. Joyce and M. Shaposhnikov, Primordial Magnetic Fields, Right Electrons, and the Abelian Anomaly, *Phys. Rev. Lett.* **79**, 1193 (1997).
 - [13] Y. Akamatsu and N. Yamamoto, Chiral Plasma Instabilities, *Phys. Rev. Lett.* **111**, 052002 (2013).
 - [14] Y. Hirono, D. E. Kharzeev, and Y. Yin, Self-similar inverse cascade of magnetic helicity driven by the chiral anomaly, *Phys. Rev. D* **92**, 125031 (2015).
 - [15] J. Schober, T. Fujita, and R. Durrer, Generation of chiral asymmetry via helical magnetic fields, *Phys. Rev. D* **101**, 103028 (2020).
 - [16] C. Manuel and J. M. Torres-Rincon, Dynamical evolution of the chiral magnetic effect: Applications to the quark-gluon plasma, *Phys. Rev. D* **92**, 074018 (2015).
 - [17] V. Domcke, Y. Ema, K. Mukaida, and R. Sato, Chiral anomaly and Schwinger effect in non-abelian gauge theories, *J. High Energy Phys.* **03** (2019) 111.
 - [18] V. Domcke, Y. Ema, and K. Mukaida, Chiral anomaly, Schwinger effect, Euler-Heisenberg Lagrangian and application to axion inflation, *J. High Energy Phys.* **02** (2020) 055.
 - [19] M. Giovannini and M. E. Shaposhnikov, Primordial hypermagnetic fields and triangle anomaly, *Phys. Rev. D* **57**, 2186 (1998).
 - [20] M. Giovannini and M. E. Shaposhnikov, Primordial Magnetic Fields, Anomalous Isocurvature Fluctuations and Big Bang Nucleosynthesis, *Phys. Rev. Lett.* **80**, 22 (1998).
 - [21] M. Dvornikov and V. B. Semikoz, Leptogenesis via hypermagnetic fields and baryon asymmetry, *J. Cosmol. Astropart. Phys.* **02** (2012) 040; **08** (2012) E01(E).
 - [22] H. Tashiro, T. Vachaspati, and A. Vilenkin, Chiral effects and cosmic magnetic fields, *Phys. Rev. D* **86**, 105033 (2012).
 - [23] A. J. Long, E. Sabancilar, and T. Vachaspati, Leptogenesis and primordial magnetic fields, *J. Cosmol. Astropart. Phys.* **02** (2014) 036.
 - [24] T. Fujita and K. Kamada, Large-scale magnetic fields can explain the baryon asymmetry of the Universe, *Phys. Rev. D* **93**, 083520 (2016).
 - [25] K. Kamada and A. J. Long, Baryogenesis from decaying magnetic helicity, *Phys. Rev. D* **94**, 063501 (2016).
 - [26] K. Kamada and A. J. Long, Evolution of the baryon asymmetry through the electroweak crossover in the presence of a helical magnetic field, *Phys. Rev. D* **94**, 123509 (2016).

- [27] P. Pavlović, N. Leite, and G. Sigl, Chiral magnetohydrodynamic turbulence, *Phys. Rev. D* **96**, 023504 (2017).
- [28] J. Schober, I. Rogachevskii, and A. Brandenburg, Production of a Chiral Magnetic Anomaly with Emerging Turbulence and Mean-Field Dynamo Action, *Phys. Rev. Lett.* **128**, 065002 (2022).
- [29] J. Schober, I. Rogachevskii, and A. Brandenburg, Dynamo instabilities in plasmas with inhomogeneous chiral chemical potential, *Phys. Rev. D* **105**, 043507 (2022).
- [30] J. García-Bellido, D. Grigoriev, A. Kusenko, and M. Shaposhnikov, Nonequilibrium electroweak baryogenesis at reheating after inflation, *Phys. Rev. D* **60**, 123504 (1999).
- [31] K. Kamada, Return of grand unified theory baryogenesis: Source of helical hypermagnetic fields for the baryon asymmetry of the universe, *Phys. Rev. D* **97**, 103506 (2018).
- [32] V. Domcke, K. Kamada, K. Mukaida, K. Schmitz, and M. Yamada, Wash-In Leptogenesis, *Phys. Rev. Lett.* **126**, 201802 (2021).
- [33] M. Yoshimura, Unified Gauge Theories and the Baryon Number of the Universe, *Phys. Rev. Lett.* **41**, 281 (1978); **42**, 746(E) (1979).
- [34] S. Dimopoulos and L. Susskind, On the baryon number of the universe, *Phys. Rev. D* **18**, 4500 (1978).
- [35] D. Toussaint, S. Treiman, F. Wilczek, and A. Zee, Matter - antimatter accounting, thermodynamics, and black hole radiation, *Phys. Rev. D* **19**, 1036 (1979).
- [36] S. Weinberg, Cosmological Production of Baryons, *Phys. Rev. Lett.* **42**, 850 (1979).
- [37] S. M. Barr, G. Segre, and H. Weldon, The magnitude of the cosmological baryon asymmetry, *Phys. Rev. D* **20**, 2494 (1979).
- [38] A. Ohnishi and N. Yamamoto, Magnetars and the chiral plasma instabilities, [arXiv:1402.4760](https://arxiv.org/abs/1402.4760).
- [39] D. Grabowska, D. B. Kaplan, and S. Reddy, Role of the electron mass in damping chiral plasma instability in Supernovae and neutron stars, *Phys. Rev. D* **91**, 085035 (2015).
- [40] Y. Masada, K. Kotake, T. Takiwaki, and N. Yamamoto, Chiral magnetohydrodynamic turbulence in core-collapse supernovae, *Phys. Rev. D* **98**, 083018 (2018).
- [41] M. Dvornikov, V. B. Semikoz, and D. D. Sokoloff, Generation of strong magnetic fields in a nascent neutron star accounting for the chiral magnetic effect, *Phys. Rev. D* **101**, 083009 (2020).
- [42] J. Matsumoto, N. Yamamoto, and D.-L. Yang, Chiral plasma instability and inverse cascade from nonequilibrium left-handed neutrinos in core-collapse supernovae, *Phys. Rev. D* **105**, 123029 (2022).
- [43] K. Kamada, N. Yamamoto, and D.-L. Yang, Chiral effects in astrophysics and cosmology, *Prog. Part. Nucl. Phys.* **129**, 104016 (2023).
- [44] V. Domcke and K. Mukaida, Chiral anomaly, Schwinger effect, Euler-Heisenberg Lagrangian and application to axion inflation, *J. Cosmol. Astropart. Phys.* **11** (2018) 020.
- [45] B. A. Campbell, S. Davidson, J. R. Ellis, and K. A. Olive, On the baryon, lepton flavor and right-handed electron asymmetries of the universe, *Phys. Lett. B* **297**, 118 (1992).
- [46] D. Bödeker and D. Schröder, Equilibration of right-handed electrons, *J. Cosmol. Astropart. Phys.* **05** (2019) 010.
- [47] D. Jiménez, K. Kamada, K. Schmitz, and X.-J. Xu, Baryon asymmetry and gravitational waves from pseudoscalar inflation, *J. Cosmol. Astropart. Phys.* **12** (2017) 011.
- [48] V. Domcke, B. von Harling, E. Morgante, and K. Mukaida, Baryogenesis from axion inflation, *J. Cosmol. Astropart. Phys.* **10** (2019) 032.
- [49] V. Domcke, K. Kamada, K. Mukaida, K. Schmitz, and M. Yamada, Wash-in leptogenesis after axion inflation, *J. High Energy Phys.* **01** (2023) 053.
- [50] K. Kamada, F. Uchida, and J. Yokoyama, Baryon isocurvature constraints on the primordial hypermagnetic fields, *J. Cosmol. Astropart. Phys.* **04** (2021) 034.
- [51] T. Hatori, Kolmogorov-style argument for the decaying homogeneous MHD turbulence, *J. Phys. Soc. Jpn.* **53**, 2539 (1984).
- [52] D. Biskamp and W.-C. Müller, Decay Laws for Three-Dimensional Magnetohydrodynamic Turbulence, *Phys. Rev. Lett.* **83**, 2195 (1999).
- [53] T. Kahniashvili, A. G. Tevzadze, A. Brandenburg, and A. Neronov, Evolution of primordial magnetic fields from phase transitions, *Phys. Rev. D* **87**, 083007 (2013).
- [54] A. Brandenburg and T. Kahniashvili, Classes of Hydrodynamic and Magnetohydrodynamic Turbulent Decay, *Phys. Rev. Lett.* **118**, 055102 (2017).
- [55] A. Brandenburg, K. Kamada, and J. Schober, Decay law of magnetic turbulence with helicity balanced by chiral fermions, *Phys. Rev. Res.* **5**, L022028 (2023).
- [56] D. N. Hosking and A. A. Schekochihin, Reconnection-Controlled Decay of Magnetohydrodynamic Turbulence and the Role of Invariants, *Phys. Rev. X* **11**, 041005 (2021).
- [57] D. N. Hosking and A. A. Schekochihin, Cosmic-void observations reconciled with primordial magnetogenesis, [arXiv:2203.03573](https://arxiv.org/abs/2203.03573).
- [58] H. Zhou, R. Sharma, and A. Brandenburg, Scaling of the Hosking integral in decaying magnetically dominated turbulence, *J. Plasma Phys.* **88**, 905880602 (2022).
- [59] A. Brandenburg and G. Larsson, Turbulence with magnetic helicity that is absent on average, *Atmosphere* **14**, 932 (2023).
- [60] A. Brandenburg, Hosking integral in nonhelical Hall cascade, *J. Plasma Phys.* **89**, 175890101 (2023).
- [61] P. Goldreich and A. Reisenegger, Magnetic field decay in isolated neutron stars, *Astrophys. J.* **395**, 250 (1992).
- [62] A. Vilenkin, Equilibrium parity-violating current in a magnetic field, *Phys. Rev. D* **22**, 3080 (1980).
- [63] A. Yu. Alekseev, V. V. Cheianov, and J. Fröhlich, Universality of Transport Properties in Equilibrium, Goldstone Theorem and Chiral Anomaly, *Phys. Rev. Lett.* **81**, 3503 (1998).
- [64] K. Fukushima, D. E. Kharzeev, and H. J. Warringa, Chiral magnetic effect, *Phys. Rev. D* **78**, 074033 (2008).
- [65] A. Brandenburg, K. Enqvist, and P. Olesen, Large-scale magnetic fields from hydromagnetic turbulence in the very early universe, *Phys. Rev. D* **54**, 1291 (1996).
- [66] A. Brandenburg, Y. He, T. Kahniashvili, M. Rheinhardt, and J. Schober, Relic gravitational waves from the chiral magnetic effect, *Astrophys. J.* **911**, 110 (2021).
- [67] A. Brandenburg *et al.* (Pencil Code Collaboration), The PENCIL CODE, a modular MPI code for partial differential

- equations and particles: Multipurpose and multiuser-maintained, *J. Open Source Software* **6**, 2807 (2021).
- [68] M. Rempel, Numerical simulations of quiet sun magnetism: On the contribution from a small-scale dynamo, *Astrophys. J.* **789**, 132 (2014).
- [69] See Fig. 7 of the PENCIL CODE Newsletter 2022/2; <https://github.com/pencil-code/website>.
- [70] H. K. Moffatt, *Magnetic Field Generation in Electrically Conducting Fluids* (Cambridge University Press, Cambridge, England, 1978).
- [71] R. Durrer and C. Caprini, Primordial magnetic fields and causality, *J. Cosmol. Astropart. Phys.* **11** (2003) 010.
- [72] G. Baym and H. Heiselberg, The electrical conductivity in the early universe, *Phys. Rev. D* **56**, 5254 (1997).
- [73] P. B. Arnold, G. D. Moore, and L. G. Yaffe, Transport coefficients in high temperature gauge theories. 1. Leading log results, *J. High Energy Phys.* **11** (2000) 001.
- [74] A. Brandenburg, T. Kahniashvili, and A. G. Tevzadze, Nonhelical Inverse Transfer of a Decaying Turbulent Magnetic Field, *Phys. Rev. Lett.* **114**, 075001 (2015).
- [75] N. Aghanim *et al.* (Planck Collaboration), Planck 2018 results. VI. Cosmological parameters, *Astron. Astrophys.* **641**, A6 (2020); **652**, C4(E) (2021).
- [76] R. L. Workman *et al.* (Particle Data Group), Review of particle physics, *Prog. Theor. Exp. Phys.* **2022**, 083C01 (2022).
- [77] A. Brandenburg, K. Kamada, K. Mukaida, K. Schmitz, and J. Schober, Datasets for Chiral Magnetohydrodynamics with Zero Total Chirality, [10.5281/zenodo.8267336](https://zenodo.org/record/8267336) (v2023.08.20); see also <http://norlx65.nordita.org/~brandenb/proj/0Chir>.
- [78] A. Brandenburg and K. Subramanian, Minimal tau approximation and simulations of the alpha effect, *Astron. Astrophys.* **439**, 835 (2005).